

The Effect of Large-Scale Power on Simulated Spectra of the Ly α forest

David Tytler*, Pascal Paschos, David Kirkman, Michael L. Norman, and Tridivesh Jena

Center for Astrophysics and Space Sciences, University of California San Diego, La Jolla, CA, 92093-0424

7 September 2021

ABSTRACT

We explore the effects of size of the box that we use for simulations of the intergalactic medium (IGM) at redshift two. We examine six simulations from the hydrodynamic code ENZO using the same cosmological and astrophysical input parameters and cell size, but different box size. We study the CDM distribution and many statistics of the Ly α forest absorption from the IGM. Larger boxes have fewer pixels with significant absorption (flux < 0.96), more pixels in longer stretches with little or no absorption, and they have wider Ly α lines. The larger boxes differ only because they include power from long wavelength modes that do not fit inside the periodic conditions of the smaller boxes. The long modes change the density, velocity and temperature fields and these increase in the gas temperature. Small simulations are too cold compared to larger ones. When we deliberately increase the heat we put into the IGM, we can approximate the Ly α forest in a simulation of twice the size. When we double the box size, the difference of most statistics from their value in our largest 76.8 Mpc box is reduced by approximately a factor of two. Most of the statistics converge towards their value in the simulation with the largest box size, though line widths are not yet converged and the most common value of the CDM density shows no sign of converging, because the larger boxes include places with ever higher densities. These regions are not in the IGM, but they may produce the strongest of Ly α lines.

When we double the box size from 38.4 Mpc to 76.8 Mpc, the mean Ly α absorption decreases 0.5%, the frequency with which we encounter different common CDM densities changes by 2%, typical Ly α line widths, the frequency of flux values and the power spectrum of the flux all change by 4–7%, and the column density distribution changes by up to 15%. When we compare to the errors in data, we find that our 76.8 Mpc box is larger than we need for the mean flux, barely large enough for the column density distribution and the power spectrum of the flux, and too small for the line widths that increase by 1 km s $^{-1}$ when we increase the box from 38.4 Mpc to 76.8 Mpc, which is approximately the error in data. We can most readily see the effects of the long wavelength modes in measurement on the smallest scales in the Ly α forest, the line widths, because they are easier to measure than the long wavelength power. Our optically thin simulations have a factor of several too few lines with H I column densities $> 10^{17}$ cm $^{-2}$. Reducing the cell size from 75 to 18.75 kpc is not a solution. Our simulated spectra have 20% less power than data on small scales and 50% less on large scales, and their Ly α lines are 2.6 km s $^{-1}$ too wide. We do not see how our simulations might match all data at $z = 2$. Reducing the cell size to 18.75 kpc lowers the Ly α line widths by 1.8 km s $^{-1}$, but radiative transfer effects can increase them by as much as 1.3 km s $^{-1}$ at $z=2.5$. We might reduce line widths using a softer ionizing spectrum to reduce heating, or we could use $\sigma_8 > 0.9$ that has the additional benefit of increasing the large scale power. It is hard to see how simulations using popular cosmological and astrophysical parameters can match the Ly α forest data at $z = 2$.

Key words: quasars: absorption lines – cosmology: observations – intergalactic medium – numerical simulations.

1 INTRODUCTION

We are exploring the physical conditions in the IGM and the history stored in those conditions. We retrieve the physical conditions by finding numerical simulations that give simulated spectra that have H I Ly α forest absorption that are statistically similar to real spectra. Data on the IGM can give relative errors of the order of a few percent for statistical properties of the forest. In Jena et al. (2005) (J05) we showed that at redshift 1.95 our simulations using typical cosmological and astrophysical parameters gave a good match to both the mean flux transmitted in the Ly α forest and the b -value distribution that we use to describes the Ly α line widths. We noted that the power spectrum of the flux for these simulations was broadly similar to that of data. However, we spent little time with the power, and we did not attempt to run any simulations that gave exactly the mean flux and b -values of data.

Here we explore one aspect of the accuracy of our simulations, the dependence on size of the simulation box. We discuss various statistics, including the mean flux, the flux probability distribution function (pdf), the typical b -value, the pdf of the b -values, the power and autocorrelation of the flux and the density and power of the CDM. We restrict our attention to one cosmological model at one epoch, and we say little or nothing about other relevant factors such as redshift evolution, the tilt of the initial power spectrum of fluctuations and a measure of the amplitude of the density fluctuations today, σ_8 . We also do not discuss other important aspects of the simulations, including the accuracy of the initial conditions, the redshift where the simulations begin (Heitmann et al. 2006; Lukic et al. 2007) the accuracy of the potential and hydrodynamical evolution (Regan et al. 2007), the ionization and heating and the lack of radiative transfer. In J50 we showed how cosmological and astrophysical parameters, and the box and cell size change the mean flux and b -values. Here we cover many more statistics of the Ly α forest in a more quantitative manner.

It is now well known (Kauffmann & Melott 1992; Pen 1997; Barkana & Loeb 2004; Sirko 2007), that we need box sizes of many hundreds of Mpc to measure the power of the matter accurately. For CDM (gravity) alone we can now run simulations that are large enough to capture most of the variations from large scale modes (Neto et al. 2007). However, we can not yet run large enough hydrodynamic simulations with the $\simeq 20$ kpc cell size required (Meiksin & White 2004) in the IGM, although we could instead run an ensemble of simulations, each with a different mean density (Mandelbaum et al. 2003). Meiksin & White (2004), for example, study the convergence properties of the flux power spectrum and autocorrelation function and recommend a box size of $25 h^{-1}$ Mpc but only for high redshifts ($z > 3$) and even then they do not find convergence to better than 10%. Similarly, (Bagla & Ray 2005) study the effects of box size on halo mass functions and indicate that a minimum box size of several $100 h^{-1}$ Mpc is needed.

A secondary goal of this work is to make it easier to obtain validated and reproducible results on the Ly α forest, in accord with the sentiments of the ‘‘Cosmic Code Comparison Project’’ (Heitmann et al. 2007). Hence we deliberately include many tables and figures to aid comparisons with other simulations.

In §2 below, we briefly describe the simulation code and parameters we have adopted. In §3 we describe the statistics of the cold dark matter distribution. §4 describes the statistics of the flux in the Ly α forest including the mean flux, flux distribution, and line b -values and column densities. In §5 we give the power of the flux spectra and the autocorrelation. In §6 we give the velocity field, baryon temperature and density. In §7 we show how putting more heat into a simulation makes its Ly α forest appear like a simulation of twice the box length. In §8 we discuss an ambiguity present in the way flux power is calculated. In §9 we discuss how cell size, or resolution changes the Ly α forest statistics. In §10 we show how the different statistics converge on the values in large boxes and we compare to data. In §11 we review the physical causes of the changes we saw with box size. The appendices contain technical details: A how we make spectra, B how we evolve them, C how we make extended sight lines, and D the lack of realistic variations in the density field.

Overall, the comparison with data shows some large differences that make it hard to see how simulations will be able to exactly match the current Ly α forest data at $z = 2$ using the popular cosmological and astrophysical parameters.

2 ENZO IGM SIMULATIONS

The numerical simulations (Bodenheimer et al. 2007) that we describe in this paper use the Eulerian hydrodynamic cosmological code ENZO (Bryan et al. 1995; Bryan & Norman 1997; Norman & Bryan 1999; O’Shea et al. 2004; O’Shea et al. 2005; Regan et al. 2007; Norman et al. 2007). The simulations contain both CDM and baryons in the form of gas, but no stars. The simulations were all run with the same cosmological parameters: a flat geometry $\Omega_{total} = 1$, comprising a vacuum energy density of $\Omega_\Lambda = 0.73$, $\Omega_m = 0.27$ (CDM plus baryons), a baryon density of $\Omega_b = 0.044$, a Hubble constant of $H_0 = 71$ km s $^{-1}$ Mpc $^{-1}$ and an initial power spectrum scalar slope of $n_s = 1.0$ with a current amplitude of $\sigma_8 = 0.9$.

The ENZO code follows the evolution of the gas using non-equilibrium chemistry and cooling for hydrogen and helium ions (Abel et al. 1997; Anninos et al. 1997). After reionization at $z = 6$, photoionization is provided using the Haardt & Madau (2001) volume average UV background (UVB) from an evolving population of galaxies and QSOs. This gives 1.330×10^{-12} photoionizations per second per H I atom at $z = 2$ and 1.041×10^{-12} photoionizations per second at $z = 3$. The simulations are optically thin so that all cells experience the same UV intensity at a given time. We do not treat the transfer of radiation inside the volume, and we include no feedback from individual stars or QSOs except for that implied by the uniform UVB.

As in J05, we use two parameters to describe the intensity of the UVB. The parameter γ_{912} is the rate of ionization per H I atom in units of the Haardt & Madau model discussed above, while X_{228} measures the heat input per He II ionization, again in units of the rate for the Haardt & Madau spectrum.

We initiate the simulations using an Eisenstein & Hu (1999) power spectrum for the dark matter perturbations, that we insert at $z = 99$. The simulated volumes are all cubes with strictly periodic boundary conditions. Hence the

power is input at a finite number of discrete wavenumbers. When we increase the box size, we insert the new modes that now fit inside the box, but we do not change the amplitudes of the smaller modes.

The amplitude of the power that we insert varies smoothly with wavenumber. We insert the amplitude expected for the universe as a whole, with no random variations associated with the finite box sizes. Since all our simulations use the same cosmological parameters, they all have exactly the same initial power for all modes that fit inside their box. The power in the simulations is not adjusted to include the variations in mean density that we see in the universe on the scale of the boxes. Hence, all the simulations are more similar to the mean of the universe than would be any observational measurement. We discuss this more in Appendix D. In this limited sense, the boxes contain information on scales much larger than their sizes.

We initiated all simulations using the same random number seed to generate the phases of all the modes. The phases are assigned to modes according to the mode direction and size measured in units of the box size (and not Mpc). Hence, in box units, the simulations have the same distribution of matter on the largest scales, as we show below.

We ran the simulations to $z = 2$, and all the results that we give refer to $z = 2$, except for specific cases discussed in Appendix B.

2.1 Series of Simulations

We will discuss three series of simulations with parameters listed in Table 1. The main A series have identical input parameters except for the box size. The larger boxes contain more total volume and mass and they contain power on scales that does not fit in the smaller boxes.

The A and KP series simulations have identical cosmological parameters and exactly the same comoving cell size of $53.25h^{-1}$ or 75 kpc comoving. Each simulation has one CDM particle for each cell initially, and each dark matter particle, in each simulation, has a mass of $M_{CDM} \simeq 9.5 \times 10^6 h^{-1} M_{\odot}$. All the simulations are fully constrained by the input parameters since we do not re-scale any of the simulations outputs, such as the densities, H I, or fluxes.

Each A and KP series simulation is a cube with side length $N \times 75$ kpc. The A series simulations differ in size by factors of two, from the largest simulation A with $N^3 = 1024^3$ cells to the smallest A7 with $N^3 = 32^3$. The A simulation has comoving box side length of $54.528h^{-1}$ or 76.8 Mpc, while the A7 has sides of $1.704h^{-1}$ or 2.4 Mpc. The box for simulation A is 32 times larger in each dimension than A7, giving it a volume $2^{15} = 32,768$ times larger. We also ran a simulation with 16^3 cells but found it significantly different and of no value to us.

We discussed simulations A, A2, A3 and A4 in J05 for other purposes. We do not use the label A5 because this was a version of A4 described by J05. In J05 we noted a problem with A2. We have now re-run this simulation and we found that the problem was incorrect joining of the sub-grids of A2 presented in J05. The results presented for A2 in J05 were incorrect for the power spectrum, but correct for the flux and b -values.

In the next few sections we discuss the A series simula-

Table 1. Parameters input to specify the simulations. Box and Cell size are comoving distances. Simulation A4 is in both the A series that explores box size and the B series that explores the cell size. The KP series are variants on the A series with different UVB intensity (γ_{912}) and heating per He II ionization (X_{228}).

Simulation or box name	N (cells)	Box size (Mpc)	Cell size (kpc)	γ_{912}	X_{228}
A	1024	76.8	75	1.0	1.8
A2	512	38.4	75	1.0	1.8
A3	256	19.2	75	1.0	1.8
A4	128	9.6	75	1.0	1.8
A6	64	4.8	75	1.0	1.8
A7	32	2.4	75	1.0	1.8
A2kp	512	38.4	75	0.9217	2.165
A3kp	256	19.2	75	0.836	2.579
A4kp	128	9.6	75	0.738	3.045
B2	512	9.6	18.75	1.0	1.8
B	256	9.6	37.5	1.0	1.8
A4	128	9.6	75	1.0	1.8
B3	64	9.6	150	1.0	1.8

tions alone. We discuss the three simulations, A2kp, A3kp and A4kp, the KP series, in §7. They explore the effect of changing the heat input per He II ionization. We discuss the 4 simulations in the B series, which include A4, in §9 when we discuss changing the resolution of the simulations by changing the cell size.

3 THE CDM DENSITY DISTRIBUTION

We discuss how the CDM density distribution varies with box size in the A series of simulations at $z = 2$. We do not discuss the baryons until §4.

In Figure 1 we show the frequency distribution of the CDM in the cells. We define the normalized-density of CDM as

$$\delta_{CDM} \equiv \rho_{CDM} / \bar{\rho}_{CDM} \quad (1)$$

where the denominator is the mean density of CDM in the universe at $z = 2$ which is also the mean density of the CDM in all our simulations. The shape of the curve is expected from semi-analytical work (Lacey & Cole 1994) on the formation of dark matter halos.

The distributions of the densities for all simulations continue towards much lower densities than we show. The distributions become steeper with decreasing density, but otherwise we see no conspicuous features. Since the simulations initially have an average of one CDM particle per cell, most cells with $\delta_{CDM} < 1$ contain no particles. Their densities can be non-zero because density is defined by distributing mass with immediately neighbouring cells whenever a particle is not exactly centred in its cell. Hence a particle at the corner of a cube would contribute $\delta_{CDM} = 0.125$ to each of the eight cells.

In Table 2 we list the percentage of the cells with zero density. This is 13.78% in simulation A, increasing systematically to 14.72% in A7. These cells have no immediate neighbours containing a CDM particle and we assigned them a nominal density of 10^{-22} particles per cell, which we can

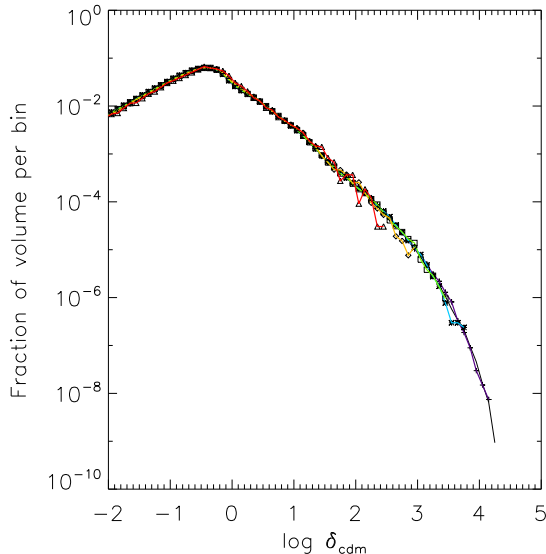


Figure 1. The frequency distribution of density of CDM, δ_{CDM} per cell. We plot the fraction of the cells (or volume) in a given simulation that have CDM density, in units of the cosmological mean density, in bins of width $\log \delta_{CDM} = 0.1$. The A simulation is shown with a solid (black) line and the other simulations are shown using a symbol in each bin, connected by straight line segments, as follows: A2 (violet pluses), A3 (blue stars), A4 (green squares), A6 (orange diamonds) and A7 (red triangles), where the larger simulations extend farther to the right.

ignore. We also list the minimum and maximum density in any cell.

The lowest density portions of the distribution are not physically realistic because we have too few particles per cell to accurately simulate densities far below the mean. We are more interested in the gravitational potential than in the density in a cell, and the potential is much smoother than the density distribution. The dark matter is smoothed twice, once when CDM is assigned to cells using the piecewise linear cloud-in-cell algorithm (Hockney & Eastwood 1988) and again when the potential is calculated. Where we have low dark matter densities, we may have low-level fluctuations in the potential due to particle discreteness. At worst, the CDM particles become mildly collisional.

The simulations in larger boxes contain higher densities, and hence they extend further to the right in Fig. 1. However, on the scale of this plot, all the simulations contain approximately the same frequencies at each density, with no variation with box size, which suggests that we will see little effect of box size on the statistics of the flux beyond those coming from the larger volumes and higher maximum densities in larger boxes. We do, however, see one minor difference between the boxes. Several simulations have frequencies lower by about a factor of two for the densities within a factor of a few of the largest value found in that simulation. This is conspicuous for A7 (red), A6 (orange) and A3 (blue), but not for A4 (green) and A2 (violet) which seem to follow A (black).

It is striking that we see almost no change with box size in the probability distribution function (pdf) of the

Table 2. Statistics of the distribution of the density of CDM in the A-series simulations. Zeros are the percentage of cells in simulation with zero density. NonL gives the percentage of cells in simulation with $\delta_{CDM} > 3$.

Name	N (cells)	Zeros (%)	Min δ_{CDM}	NonL (%)	Max δ_{CDM}
A	1024	13.78	$3.68 \cdot 10^{-11}$	4.67	$1.64 \cdot 10^4$
A2	512	14.07	$2.32 \cdot 10^{-10}$	4.68	$1.41 \cdot 10^4$
A3	256	14.37	$4.86 \cdot 10^{-9}$	4.71	$5.71 \cdot 10^3$
A4	128	14.44	$3.92 \cdot 10^{-8}$	4.79	$3.12 \cdot 10^3$
A6	64	14.67	$3.50 \cdot 10^{-8}$	4.85	$8.25 \cdot 10^2$
A7	32	14.72	$2.09 \cdot 10^{-7}$	4.91	$3.01 \cdot 10^2$

CDM density per cell for the overdensities responsible for the Ly α forest absorption, approximately $0.5 \leq \delta_{CDM} \leq 16$. We obtain the typical baryon density corresponding to a given $\log N_{HI}$ from Schaye (2001, Eqn. 10) who developed an analytic model that gives an excellent fit to simulations. Using the cosmology for the A series ($\Omega_m = 0.27$, $\Omega_b = 0.044$, $H = 71$ km/s/Mpc) and the temperature-density relation from simulation A2 ($T = 12910$ K $(\rho_b/\bar{\rho}_b)^{0.6}$, J05 Table 9) we find at $z = 2$

$$N_{HI} \simeq 7.8 \times 10^{12} (\rho_b/\bar{\rho}_b)^{1.34} \quad (2)$$

Lines in the Ly α forest with $\log N_{HI} = 12.5 - 14.5$ cm $^{-2}$ then come typically from baryon overdensities of $\rho_b/\bar{\rho}_b = 0.5 - 15.7$. A larger range of densities is involved in making significant absorption in the Ly α forest (Schaye et al. 2003). For this discussion we assume that the baryon and CDM density fluctuations are similar in amplitude. Gnedin et al. (2003) show that the baryon fluctuations are similar to the CDM fluctuations on scales larger than the filtering scale, with $\delta_b/\delta_{CDM} = \exp(-k^2/k_F^2)$, where the filtering scale k_F depends on the integral over time of the Jeans length and is approximately 0.055 s/km (11 Mpc $^{-1}$) at $z = 2$ (their Fig. 2).

The statistics on the distribution of the density of CDM in Table 2 show that both the maximum and minimum density of CDM in any cell increases systematically with the box size. The minimum is not relevant to us; since we work with the density and not the log(density), these values are all essentially zero, but the maxima are important for the flux spectra.

In Figure 2 we zoom in on the densities that are more important for the flux in the Ly α forest, and we expand the sensitivity by dividing by the frequencies found in simulation A. We now see systematic trends with box size. The larger boxes have higher frequencies of small densities, approximately $\log(\delta_{CDM}) < -0.3$, and lower frequencies of higher densities. All boxes have approximately the same frequency for $\log(\delta_{CDM}) \simeq -0.3$, near the most common density. At densities below the most common, the largest difference from the A simulation is seen at lower densities in the smaller boxes. Above the most common densities, the largest differences from A are seen at near the mean density. The larger the box, the less the deviation from A. We anticipate that these differences will manifest as changes in the baryon density and hence the Ly α forest.

In Table 3 we list two further statistics showing the changes in the CDM density per cell with box size, the RMS and the mean of the absolute difference (MAD),

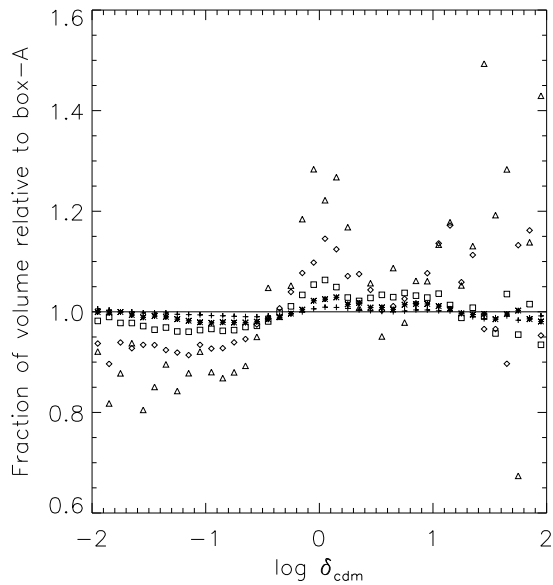


Figure 2. As Fig. 1 but showing the frequency of the densities of CDM in units of the frequency in simulation A. The points from the larger boxes are higher at $\log \delta_{CDM} = 1$.

Table 3. Statistics of the Distribution of the Density of CDM Relative to Simulation A

Name	MAD (%)	RMS (%)
A	0.00	0.00
A2	0.57	0.70
A3	1.23	1.44
A4	3.01	3.32
A6	7.11	8.23
A7	14.30	17.79

each relative to the value in to box A and averaged over $-2 < \log(\delta_{CDM}) < 2$. Both statistics decrease by about a factor of two for each doubling in box size, reaching an RMS of only 0.7% for simulation A2. We will see a similar rate of convergence for other statistics of the Ly α forest (McDonald & Miralda-Escudé 2001).

3.1 Distribution of the variance of the density of CDM amongst sight lines

We will be examining the power of the CDM in the next section because this helps us understand how the simulations in general and particularly the power of the flux change with box size. Here we look first at the variance of the CDM because this is related to the sum of the power over all modes.

In Figure 3 we show the xy faces of the series A simulations. For each position in the xy plane, we show

$$s_l^2 \equiv (1/N) \sum_z (\delta_{CDM} - 1)^2, \quad (3)$$

the mean value of $(\delta_{CDM} - 1)^2$ along the N cells parallel to the z axis which goes into the page. We consider these rows as sight lines, which we label with the subscript “ l ” to

Table 4. Statistics of the distribution s_l^2 amongst sight lines.

Name	Min	Mode	Mean	Max
A	0.61	3.55	175.78	$1.14 \cdot 10^6$
A2	0.58	1.78	146.12	$8.39 \cdot 10^5$
A3	0.50	0.71	122.84	$2.49 \cdot 10^5$
A4	0.43	0.71	100.66	$1.11 \cdot 10^5$
A6	0.36	0.71	53.38	$2.24 \cdot 10^4$
A7	0.29	0.71	26.61	$3.42 \cdot 10^3$

indicate a choice of both x and y . We show this quantity because Ns_l^2 is the contribution of that sight line to the variance of δ_{CDM} in the whole simulation box, since

$$\begin{aligned} N^3 \text{Var}(\delta_{CDM}) &\equiv \sum_{x,y,z} (\delta_{CDM} - \bar{\delta}_{CDM})^2 \\ &= \sum_{x,y,z} (\delta_{CDM} - 1)^2 = \sum_{x,y} N s_l^2, \end{aligned} \quad (4)$$

where N^3 is the number of cells in the simulation box, and $\bar{\delta}_{CDM} = 1$ if and only if it is the mean of the δ_{CDM} values of all cells in the box, following the definition of δ_{CDM} in Eqn. 1.

The quantity s_l^2 tells us how much that sight line contributes to the mean power of all sight lines. The quantity s_l^2 is not the variance along each sight line, σ_l^2 , since that is the mean of $(\delta_{CDM} - \bar{\delta}_{CDM,z})^2$, where the $\bar{\delta}_{CDM,z}$ is the mean along each sight line. These means differ from sight line to sight line, and can be very different from unity.

Figure 3 looks similar to the projection of the density, since the s_l^2 is largest where we encounter a cell with a high density. If we shrink the squares from the smaller simulations to give constant Mpc per mm on the page, then the density and size of structures looks approximately the same in all simulations, although they are not the same, for example because the smaller boxes are also smaller in the z direction.

In Figure 4 we show the distribution of the s_l^2 and in Table 4 we give some statistics. We have one s_l^2 for each sight line parallel to the z axis of each simulation box. Larger boxes have a lower frequency of sight lines with small s_l^2 , their most common (mode) s_l^2 is larger, they have a higher frequency of larger s_l^2 , and larger maximum s_l^2 . This is because the larger boxes have more sight lines, each of which is longer, and there are higher densities in the larger boxes.

The small boxes lack the high density peaks of the larger boxes because they lack volume, and they lack long modes. They do not contain enough particles to produce the highest densities. To make a peak with 10^6 particles in a cell, we must collect particles from 10^6 cells, more than are contained in the A7 simulation.

Bagla & Ray (2005) have explored how the frequency of high density CDM collapsed structures changes with effective box size. They use simulations with $N = 256$ CDM particles in $300h^{-1}\text{Mpc}$ boxes with a softening length of $0.47h^{-1}\text{Mpc}$. They find that the number of high density peaks decreases when they truncate the initial power spectra at lengths less than the full box size. They see a factor of three fewer collapsed structures with mass $10^{15}M_\odot$ when they truncate the power at 1/4 of the box size. However, when they truncate at 1/2 the box size they see only an 80% reduction in the number, showing convergence to the result

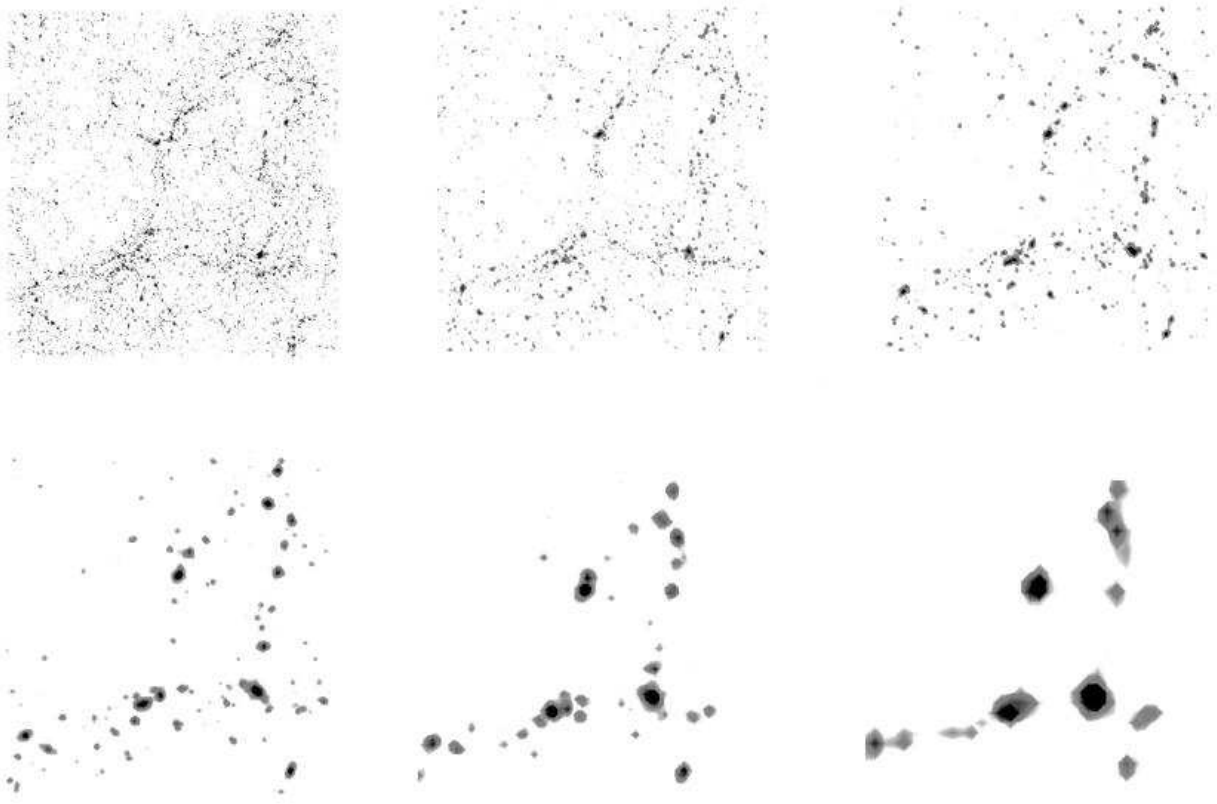


Figure 3. The contribution to the total variance of the density of CDM from each sight line. The sight lines are parallel to the z axis that goes into the page. Simulation are, from upper left to lower right, A, A2, A3, A4, A6 and A7. Pixels that have variance below the mean are shown as white. Darker pixels have larger $\log s_l^2$.

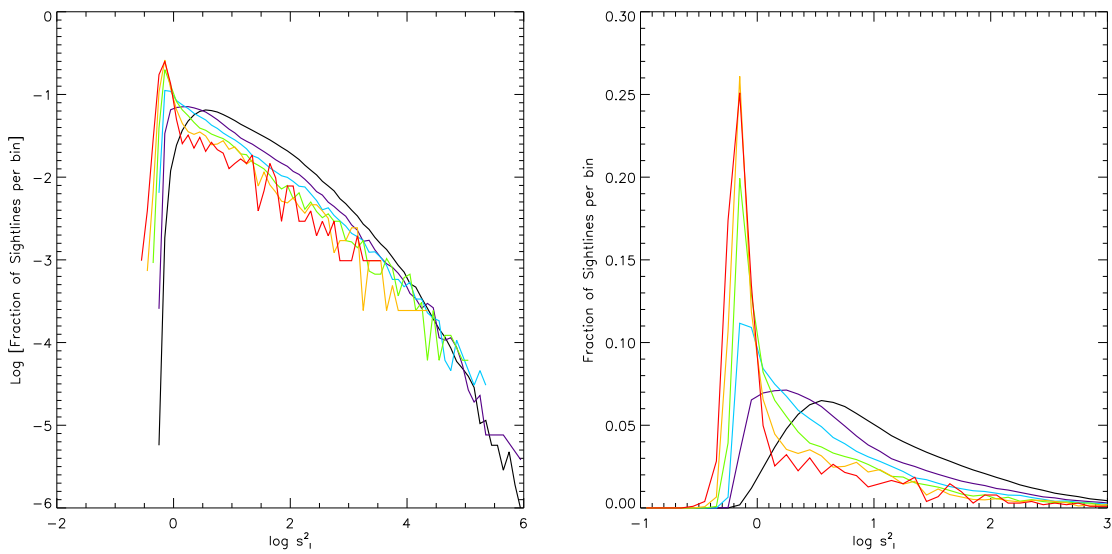


Figure 4. Distribution of the s_l^2 . The s_l^2 is measured along sight lines parallel to the z axis and of length equal to the size of each box. The vertical axis shows the fraction of sight lines (pixels in the xy plane) with variance in bins of $\log s_l^2 = 0.1$. The vertical scale is \log (fraction) on the left panel and linear fraction on the right. The larger boxes have larger modes (right panel), and extend to larger s_l^2 values (left panel). Both A and A2 have approximately the same maximum s_l^2 .

expected for a much larger box. This convergence happens for boxes 3 – 6 times larger than A.

3.2 Power of Normalised CDM Density

We compute the Fourier transform $D(k)$ of $\delta_{CDM}-1$, the normalised-density of CDM minus one,

$$D(k) = \frac{1}{(\Delta u)^{1/2}} \int_{-u}^u (\delta_{CDM}(u) - 1) e^{-jku} du$$

$$\simeq (\Delta u)^{1/2} \sum_{i=1}^{N_p} (\delta_{CDM}(u_i) - 1) e^{-jku_i} \quad (5)$$

where k is the wavenumber, i is the pixel index, u is velocity and $\Delta u = c\Delta z/(1+z)$ is the velocity width of a pixel with redshift width Δz . Subtracting one has no effect on $D(k)$ except for the mode with zero frequency. We take the transform of the density along each sight line parallel to and extending the full length of the z axis. We did not explore the x and y directions. We use a discrete Fast Fourier Transformation algorithm, and we use

$$P(k) = \langle D(k)D^*(k) \rangle \quad (\text{km s}^{-1}), \quad (6)$$

as our estimate for the one-dimensional power, where the brackets refer to averaging over all sight lines parallel to the z axis.

Since the density distributions in the box is always strictly periodic, the power spectrum (of the signal along sight lines parallel to the z axis) is non-zero for the discrete set of modes $k = 2\pi s/L_v$, where $s=1,2,3\dots N$, and $L_v = LH(z)/(1+z)$ is the length of each spectrum in velocity units, corresponding to L comoving Mpc. At redshift $z = 2$, $H = 201.069 \text{ km s}^{-1}\text{Mpc}^{-1}$, and simulation A has $L_v = 5147.37 \text{ km s}^{-1}$.

In Figure 5 we show the power spectrum of $\delta_{CDM}-1$ for the A series boxes. We begin each spectrum at the left at its fundamental mode, the smallest wavenumber $k_{box} = 2\pi/L_v$ for that box. For simulation A $k_{box} = 2\pi/L_v = 1.22066 \times 10^{-3} \text{ s/km}$. We end the plots on the right at the Nyquist frequency, $k_{cell} = 2\pi/(2L_{cell}) = 0.682 \text{ s/km}$, or $\log k_{cell} = -0.20 \text{ s/km}$, where L_{cell} is the velocity width of a simulation cell, 5.027 km s^{-1} at $z = 2$.

The power is larger at all k in the larger boxes, which we expect because the variance like quantity s_l^2 in Fig. 4 is also larger. The increase in power with box size is most pronounced on the largest scales. The power is larger in larger boxes even on the smallest scales. We now present a figure that shows that the increase in the power with box size is intrinsic to the density distribution, and not an artifact of the length of the sight lines or the number of sight lines through the boxes.

In Figure 6 we show power spectra obtained from simulation A6 using a reduced number of shorter sight lines. We divide the A6 cube into the eight sub-cubes, each of size A7, that together exactly fill A6. We made spectra from all the sight lines restricted to each sub-cube, and we took the power spectrum of each. We then distribute these power spectra randomly into the eight means, each of which contains some sight lines for each of the eight sub-cubes, and the same total number of sight lines as does the mean power spectrum of A7. We see that the power in the sub-cubes is distributed about that in A6, and not A7. This shows that

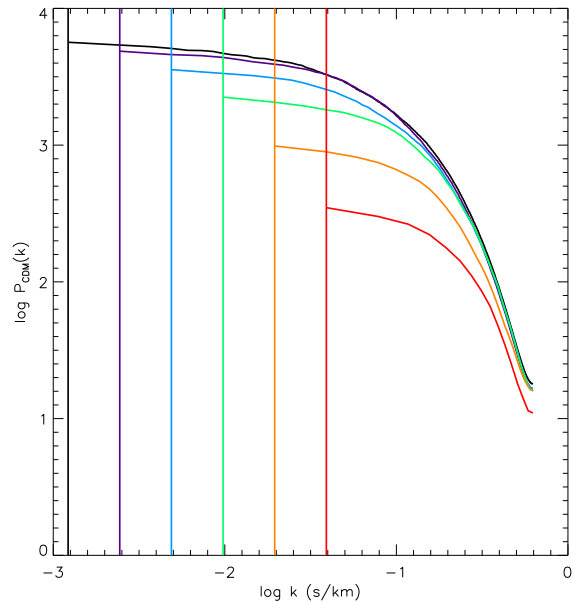


Figure 5. The 1D power spectra of $\delta_{CDM}-1$, taken along all 1D line of sight lines parallel to the z axis of each A series box. The vertical lines show the largest modes for each box, those with $k_{box} = 2\pi/L_v$. The power for the larger box are larger and extend farther to the left (large distances).

the extra power in A6 is intrinsic to the density distribution in A6, and not from the length or number of sight lines. The dispersion of the power in the 8 spectra gives one indication of the random error in the power of the A7 simulation.

3.3 Power from Density Peaks

Parseval’s Theorem states that sum of the power at all modes is proportional to the sum of the square of the signal. Using the signal from Eqn. 4, we have

$$\frac{1}{N^3} \sum_{x,y,z} (\delta_{CDM} - 1)^2 = \frac{k_{box}}{2\pi} \sum_k P(k) = \frac{1}{2\pi} \int_k P(k) dk \quad (7)$$

where N^3 is the number of cells in a box, and $P(k)$ has velocity units that cancel the inverse velocity units on the k_{box} . This can also be written as

$$\frac{1}{N^2} \sum_{x,y} s_l^2 = \frac{1}{L_v} \sum_k P(k), \quad (8)$$

which shows that the mean value of s_l^2 averaged over all cells in the box, is equal to the sum of all modes in the power (which is also averaged over all sight lines), divided by the length of each spectrum. This is the normalisation used by McDonald et al. (2006) (Eqn. 12). It is the “System 2” normalisation from Bracewell (1986) (p. 7).

The s_l^2 values show how the sum of the power at all modes is distributed amongst the sight lines. We saw in Fig. 4 and Table 4 that a few sight lines have s_l^2 values vastly larger than the mean. This means that these few sight lines also dominate the total power of each simulation.

In Figure 7 we show a single 1024 pixel line of sight from simulation A with a density peak of $\delta_{CDM} \simeq 3 \times 10^3$. This

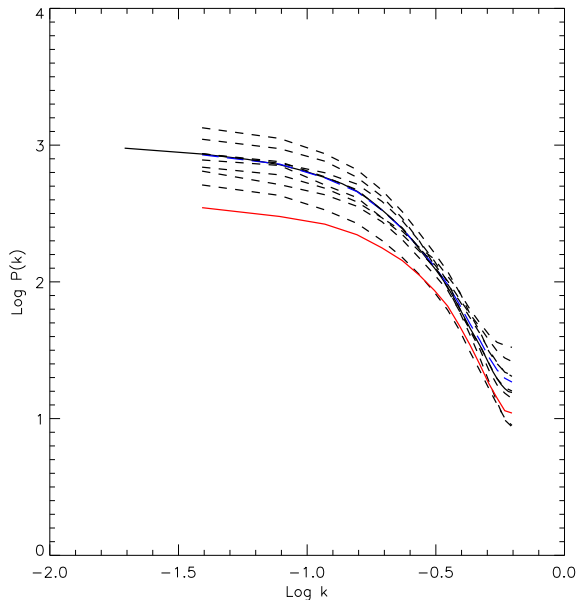


Figure 6. The 1D power spectra of δ_{CDM-1} for sight lines of length 64 cells drawn from the A6 (128^3) simulation. The solid (black) line extending farthest to the left is the power for all sight lines through A6. The eight short dashed lines show the power for sub-samples, each with 64^2 sight lines of length 64 cells. The lowest lines on the left (short solid red) is the power for the A7 box, which also comprises 64^2 sight lines each of length 64 cells.

peak increases the power about 1000 times over a wide range of wavenumbers. The density spike is narrow in velocity space, and hence wide in k space (e.g. Fig. 6.2 of Bracewell (1986)). In the lower right panel we see that smoothing the density spike removes most of the excess power.

We can estimate the amount of power added quantitatively. A typical sight line from simulation A has s_l^2 of order 3 (Table 4). One pixel with a normalised-density of 1700 increases the variance to $(3 \times 1023 + 1700^2)/1024 = 2800$, approximately the increase we see in the integrated power. Hence, a single sight line with a normalised-density $\delta_{CDM} = 10^6$ will contain as much power as the whole cube of 10^9 sight lines each with typical variance. Simulation A contains 77 cells with $\delta_{CDM} > 10^5$ and 12 with $\delta_{CDM} > 10^{5.5}$, sufficient that these few cells, and the sight lines that pass through them, will dominate the power spectrum of the (un-smoothed) CDM.

In Figure 8 we show how the sum of the s_l^2 of the sight lines increase with the number of sight lines included. We start on the left with the sight lines with the smallest s_l^2 , ending on the right with those with the largest. We see that, for all simulations, the few sight lines with the largest s_l^2 completely dominate the total. Depending on the simulation, 90% of the total s_l^2 comes from only 2 to 10% of the sight lines. The total s_l^2 , and hence the total power, is an unstable quantity, which can change significantly as the few highest density peaks changes in number and density.

We have shown that the power of the CDM density is larger in larger boxes primarily because larger boxes contain rare regions with higher density. We also see higher power because we use longer sight lines in the larger boxes. As

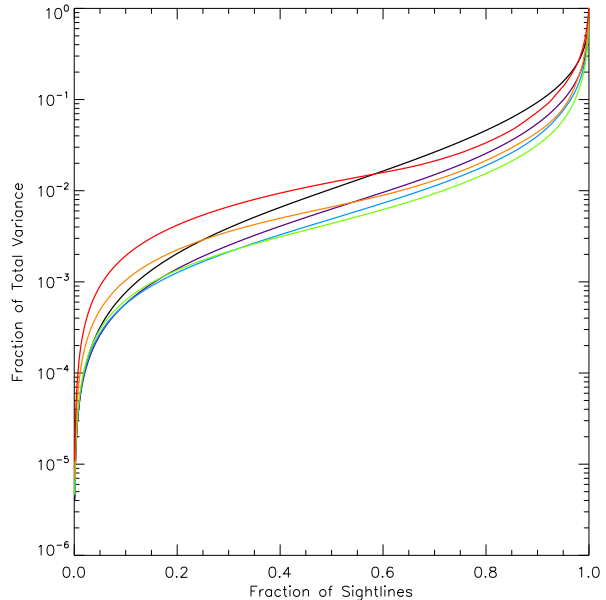


Figure 8. The cumulative sum of the contribution of the sight lines through a simulation to the total power of all sight lines. The vertical axis is the cumulative sum of s_l^2 . The horizontal axis shows the rank of the sight line ordered in increasing s_l^2 , which is its contribution to the total variance. We express the rank as a fraction of the total number of sight lines, to simplify comparison of the simulations. The vertical axis is the sum of the s_l^2 in all sight lines with s_l^2 smaller than indicated on the horizontal axis, divided by the total s_l^2 . From top to bottom at a fraction of 0.8 the boxes are A (black), A7 (red), A2 (violet), A6 (orange), A3 (blue) and A4 (green).

Bagla & Ray (2005) showed, there is some effect from having longer modes in the larger boxes. However, Figs. 1, 2 showed only small changes in the frequencies of different densities per cell, which suggest that the extra long modes have a small effect on the quantities that we are evaluating.

When we examine the flux transmitted through the IGM we are most interested in densities near the mean. Although the larger boxes have higher maximum densities, they have slightly lower portions of their volume above a moderate density. In Table 2 the column NonL gives the fraction of cells with CDM density exceeding 3 times the mean. This fraction decreases systematically with box size, from 4.91% for A7 to 4.67% for A.

4 STATISTICS OF THE FLUX IN THE Ly α FOREST

We make flux spectra using code described in Zhang et al. (1997) and J05. We make each spectrum along a row of cells parallel to the z axis of the boxes, just as we did for the s_l^2 values that describe the variance of δ_{CDM} in §3.1. We use a number of pixels equal to the box side length N .

In Figure 9 we show spectra of the flux along some random, unrelated sight lines through the A series simulations. We show equal total velocity length for all simulations, and hence for A7 we show 32 disjoint spectra, each separated by a vertical dotted line. We should ignore the vertical discon-

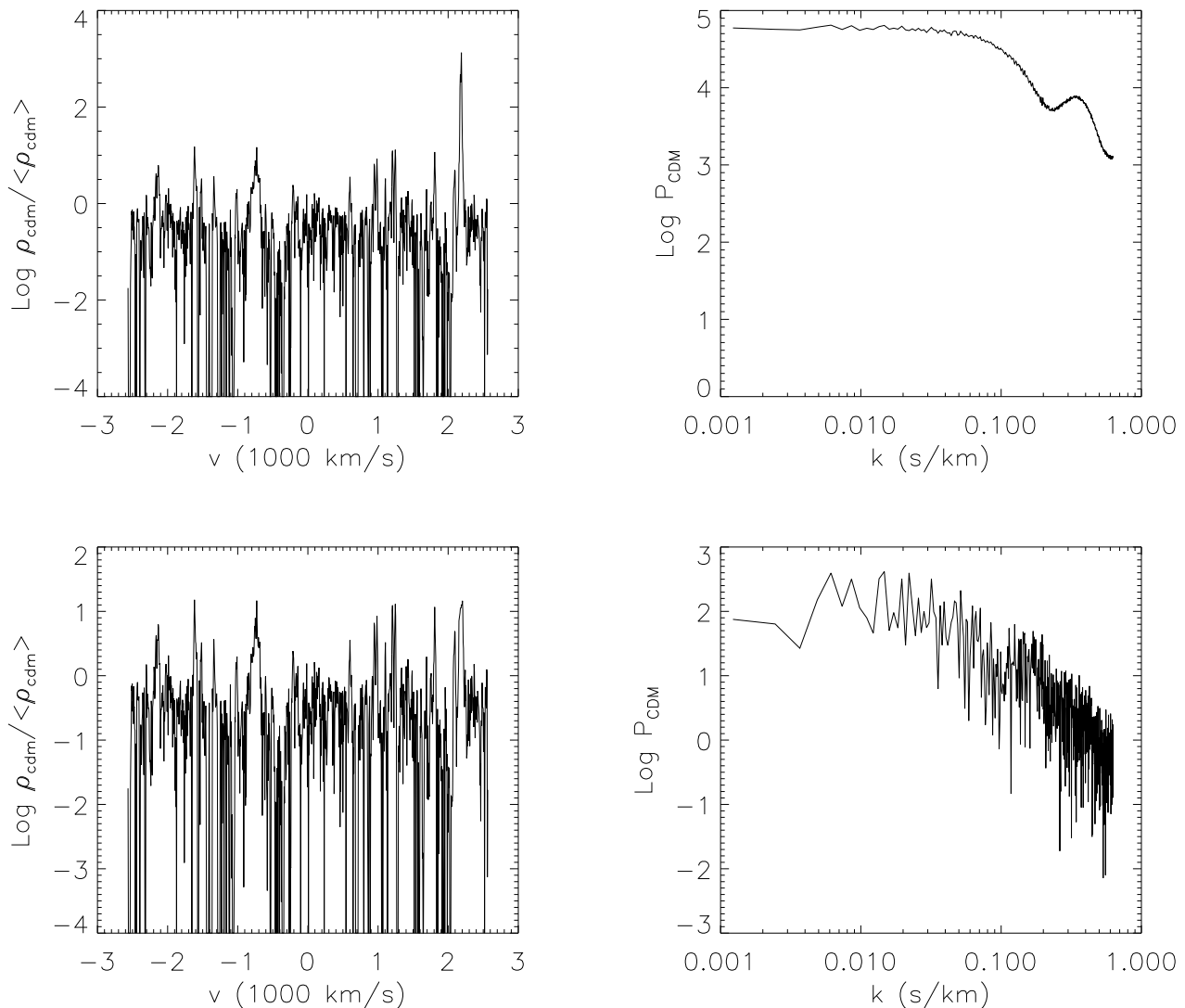


Figure 7. The normalised-density of CDM δ_{CDM} along a single sight line (208) in simulation A as a function of velocity in the full length through the box (top left). On the top right we show the 1D power spectrum of this normalised-density. In the lower left panel we have removed the density peak by smoothing the CDM between 2200 and 2250 km s^{-1} with a box car average of 20 pixels or 100 km/s . The corresponding power is on the lower right. We show the log of the normalised-density to show both the typical variations and the peak. We take the power of the linear, not the log normalised-density. The vertical scale on the two lower panels is different from on the corresponding upper panels.

tinuities where spectra end inside an absorption line. These tend to make lines look narrower, especially in the smaller boxes where there are more discontinuities. We see two major trends with box size.

The larger boxes contain large velocity intervals with very little absorption. These stretch over many hundreds of km/s , longer than the size of the smaller boxes. The larger the box, the longer the regions with little absorption. These low absorption regions are clearly showing correlation in the density on large scales. We would not expect to see them as often if we truncated the power to include only short modes.

The smaller boxes seem to have more absorption in total. The values that we list in the figure caption show this is correct for the A6 and A7, but the larger simulations have

nearly identical mean flux. The smaller simulations also have a higher proportion of pixels with flux within a few percent of the continuum, and they have fewer lines of depth 5 – 50%. The number of the deepest lines seems approximately constant.

4.1 Statistics of Flux Spectra

In Table 5 we list statistics of the flux for the spectra from the simulations. The statistics are from each pixel in all N^2 spectra through each box in the z direction. The Δ values are the mean flux that we should add onto the current value to obtain that in the next larger box. The overall trend of the mean flux \bar{F} with box size is hard to discern because

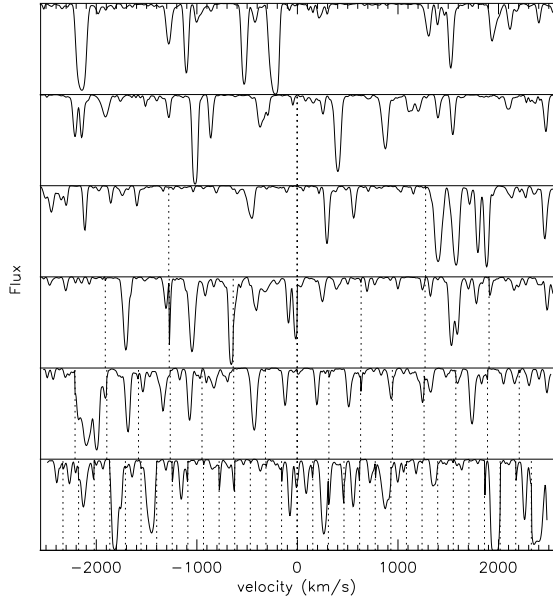


Figure 9. Spectra of the flux from sight lines drawn from the A series simulations, with the largest, A at the top, A2 next through A7 the smallest at the bottom. All are shown on the same velocity scale to aid comparison of line widths. To fill the length of simulation A, we show 2 disjoint, unrelated spectra for simulation A2, separated by the vertical line in the middle. For simulation A7 we show 32 randomly chosen spectra from this 32^3 box. When the end of a spectrum occurs in an absorption line we see a vertical discontinuity in the plot. Averaging along the spectra shown, the mean fluxes are 0.887, 0.907, 0.900, 0.891, 0.870 and 0.821 from the largest to the smallest box.

Table 5. Statistics of the flux in all spectra from the simulations. We list the mean flux, the error on the mean, the change in the mean to obtain the flux in the next larger box and the normalised variance of the transmitted flux. These statistics all refer to the flux in each pixel in the box. The column $\text{Mode}(\bar{F}_L)$ is different and refers to the mean flux per sight line, (\bar{F}_L) , rather than per pixel. The Mode is the most common of the mean flux values in bins of 0.0005.

Name	\bar{F}	error	Δ	$\text{Var}(F/\bar{F})$	$\text{Mode}(\bar{F}_L)$
A	0.8714	0.0039	0.051	0.8875
A2	0.8721	0.0059	-0.0007	0.058	0.9075
A3	0.8734	0.0113	-0.0013	0.060	0.9325
A4	0.8741	0.0168	-0.0007	0.067	0.9375
A6	0.8612	0.0332	0.0129	0.073	0.9575
A7	0.8335	0.0531	0.0277	0.095	0.9725
A2kp	0.8716	0.0059	-0.0002	0.058	0.9075
A3kp	0.8707	0.0118	0.0009	0.058	0.9275
A4kp	0.8701	0.0181	0.0006	0.063	0.9325

the changes are small compared to the measurement errors (discussed below). The underlying trend is apparently for larger mean flux in larger boxes, but this seems to reverse for the largest 4 boxes, where the flux decreases in the larger boxes.

We estimated the errors on the mean flux values in Table 5 from the standard deviation of the mean flux values for tiles across the xy face of each box. We use tiles of con-

tinuous area because the spectra in adjacent sight lines are highly correlated, and hence the error on the mean flux value is much larger than the standard deviation divided by the square root of the number of samples. We use a 4x4 tiling for A and A2, 3x3 for A3 and A4 and 2x2 for A6 and A7. These choices are a compromise between having enough tiles to give a small random error and having tiles large enough to reduce the inter-tile correlations.

The error given by tiling captures some of the variation in the mean density on large scales across the boxes. However it is less than the external error that we would want to use when we compare to real spectra because it misses all of the variation that we would see if we started each box with different random phases, and we allowed each mode to have a random amplitude, and it misses the variation due to all modes larger than the box. On the other hand, this error from tiling is larger than the smallest change that we can consider indicative of a trend when we compare a series of boxes. This is because the statistics are evaluated from the whole of each box and all boxes use the same amplitudes and phases for their modes.

In Table 5 we also list the variance of the flux F/\bar{F} evaluated for all sight lines through the box, where \bar{F} is the mean flux in the box, and not that in each sight line. We have $\text{Var}(F/\bar{F}) = N^{-3} \sum ((F/\bar{F}) - 1)^2$, where the sum is over all N^3 pixels from all spectra though one side of the box. The variance of the flux in each pixel is then $\text{Var}(F) = \bar{F}^2 \times \text{Var}(F/\bar{F})$. The $\text{Var}(F/\bar{F})$ quantity decreases systematically with increasing box size, because, we will now see, the fraction of pixels with flux < 0.97 is up to a factor of two smaller in the larger boxes.

In Figure 10 we show the distribution of the flux per pixel for all spectra through each A series simulation, also called the flux pdf. In Figure 11 we show the same value, divided by the fractions for simulation A. The simulations all have approximately the same frequency of pixels with a flux of 0.96 – 0.97. The larger simulations have higher frequencies above 0.97, and lower below. Our impression that the spectra from the smallest boxes have more absorption is confirmed; they do have a much larger fraction of pixels with $0.05 < \text{Flux} < 0.9$. We also confirm that the larger simulations have more pixels with very high flux. We see smaller changes between the larger simulations, indicating convergence by the size of box A. If this trend continues, then the fractions for simulation A will be within approximately 5% of those for a much larger simulation.

We see that the differences between the simulations decrease to less than 10% for fluxes below 0.02; they all have the same fraction of their spectra occupied by the bottoms of saturated absorption lines. This is reasonable because Figs. 1 and 2 show they all have approximately the same frequency (per Mpc^3) of high density regions. The largest differences between the boxes are for intermediate flux levels from the sides of saturated lines, or the bottoms of nearly saturated lines, both of which are a small fraction of the pixels.

In Table 5 we also list $\text{Mode}(\bar{F}_L)$ the mode of the mean flux values, \bar{F}_L , with one mean per sight line. The modes are the most common mean fluxes when we use bins of 0.0005. In contrast with the mean flux per pixel, these modes per sight line show a systematic decrease with increasing box size. These modes are all much less than the mode of the flux in

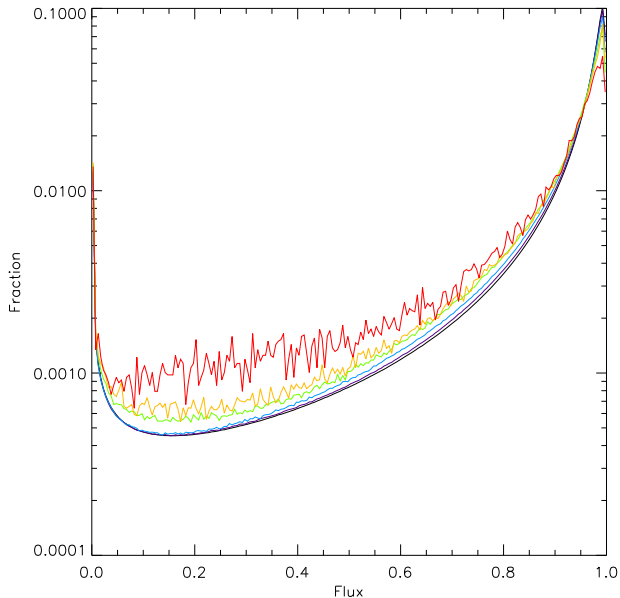


Figure 10. The distribution of the flux per 5 km s^{-1} pixel in the spectra from the A series simulations. We use 200 bins for the flux, each of size 0.005. The distribution from the larger boxes are lower on the plot for most fluxes ($0.2 < \text{flux} < 0.9$).

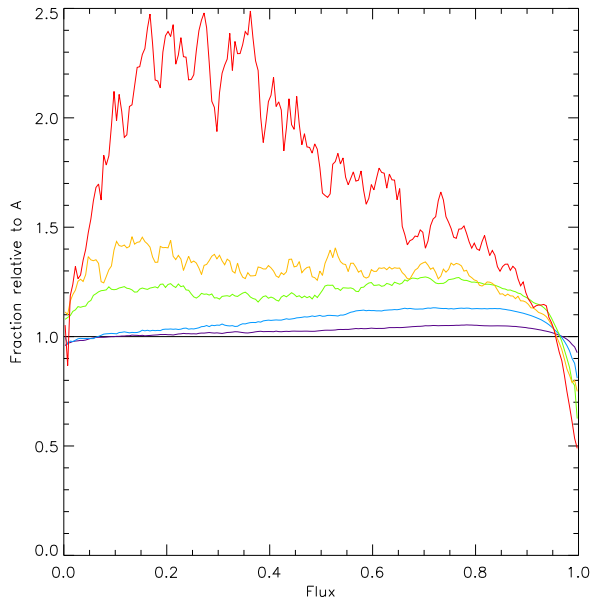


Figure 11. Distribution of the flux per pixel for A series. We show the fraction of pixels divided by those for simulation A. The results for larger boxes are nearer to the horizontal line at 1.0 for most flux values.

individual pixels, which is 0.990 to 0.995 for all boxes, as seen in Fig. 10.

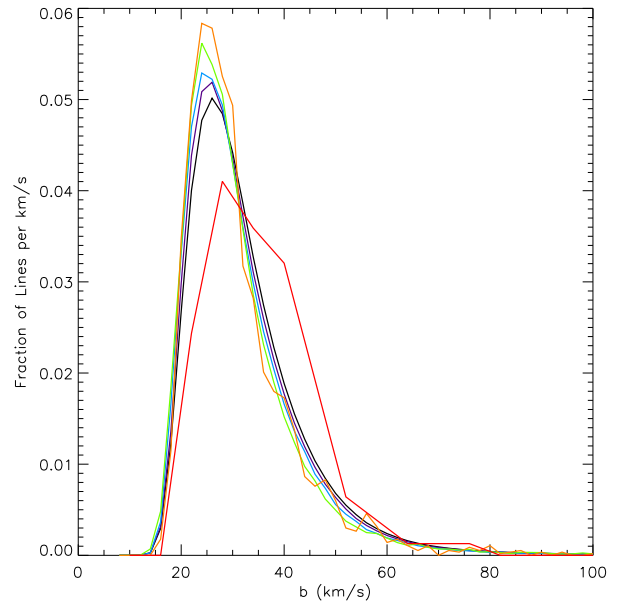


Figure 12. The distribution of the b -values for the lines with $12.5 < \log N_{\text{HI}} < 14.5 \text{ cm}^{-2}$ and $\tau > 0.05$ from the A series simulations. We show the fraction of all lines that are in 2 km s^{-1} wide bins (centred at 20, 22, 24 km s^{-1} etc.), or 6 km s^{-1} for A7. The corresponding best estimate b_{σ} values are shown in Table 6. The results from the larger boxes are lower at $b = 25 \text{ km s}^{-1}$, with the exception of the lowest curve which is from the smallest box.

4.2 Statistics of the Lines

In this section we quantify the types of lines seen in the simulations. We obtain line statistics by fitting Voigt profiles as described in Zhang et al. (1997). As in Tytler et al. (2004) and J05 (§5.1, 6.2) we consider only lines with $12.5 < \log N_{\text{HI}} < 14.5 \text{ cm}^{-2}$. We also limit our discussion to lines with central optical depths $\tau > 0.05$, which is a new constraint for this paper.

4.2.1 Line Widths: b -values

In Figure 12 we show the distribution of the b -values. The distributions show small but clearly systematic changes with box size. In detail, the larger boxes have wider lines, fewer narrow lines with $b < 28 \text{ km s}^{-1}$, and more lines with $b > 28 \text{ km s}^{-1}$, and a slightly broader distribution. The smallest box A7 is an exception to this, presumably because the fundamental mode in this box is nonlinear at $z = 2$. The change in typical line width can come from a combination of three factors: larger absorbing regions, giving more Hubble flow across a line; larger peculiar velocities from the increase in large scale power; and higher temperatures also from the increase in velocities (Theuns et al. 1999; Bryan et al. 1999).

In Fig. 13 we see that the b -value distribution is sensitive to the minimum line central optical depth τ . We use a sample with $12.5 < \log N_{\text{HI}} < 14.5 \text{ cm}^{-2}$ and $\tau > 0.05$. If instead we use a sample with $\tau > 10^{-5}$ we see a different b -value distribution that has a larger fraction of lines with $b < 27 \text{ km s}^{-1}$ and a smaller fraction of lines with larger b -values. Our sample is the subset of the total which

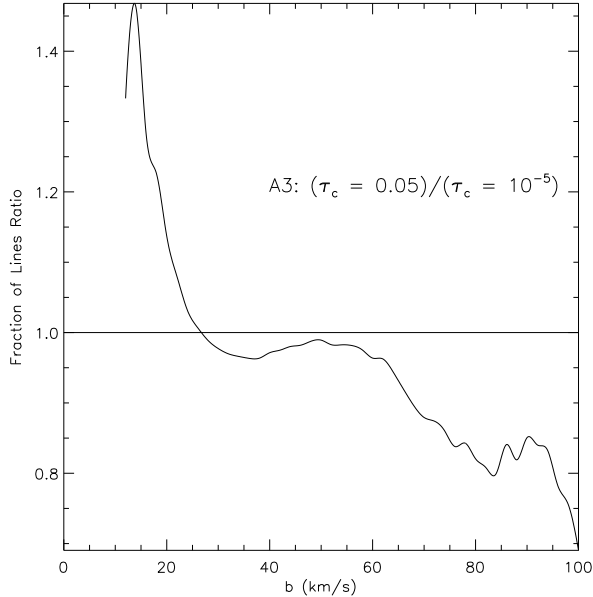


Figure 13. The b -parameter distribution for the A3 box. The vertical axis is the ratio of the fraction of lines in two samples, the sample with $\tau > 0.05$ divided by the fraction for the sample with $\tau > 10^{-5}$. We find all lines with $\log N_{\text{HI}} > 12.5$ (cm^{-2}) and plot the ratio of the fraction of lines which have $\tau > 0.05$ with the fraction of lines which have $\tau > 10^{-5}$ as a function of the b -value of the line.

lacks broad shallow lines. The shape of the distribution in the figure comes from the simultaneous requirement that $\log N_{\text{HI}} > 12.5$ (cm^{-2}) and $\tau > 0.05$. Narrow lines with $\log N_{\text{HI}} > 12.5$ always have $\tau > 0.05$ and hence they are not effected by the 0.05 limit. Very broad lines often have $\log N_{\text{HI}} > 12.5$ and $\tau < 0.05$.

In Tytler et al. (2004, Fig. 18) we showed that Hui & Rutledge (1999) function gave an excellent fit to the distribution of b -values from a simulation B, which had 35 kpc cell size, half of that used here. The Hui-Rutledge function has only one parameter, the b_σ that describes the typical line width.

In Table 6 we give estimates for the b_σ values that best fit the distributions of the lines from each simulation. We use the maximum likelihood method since it treats the individual b -values, and not the binned values that we show in the plots. We make two improvement on J05. First, we now fit only lines with $b < 40$ km s^{-1} because we want b_σ to describe the most common lines, and not the rare broad features that are hard to see in real spectra because of photon noise, flux calibration problems and uncertain continua. When we included all b -values in J05 the b_σ was larger by about 0.5 km s^{-1} . Second, we completely sample the boxes, where as J05 had few spectra, all of which began at the lowest density part of that box. The values that we give here differ from those that we gave in J05 for the same simulations for these reasons. We estimate the errors using the tiles, as we did for the for the mean flux, and again the same comment apply; external errors are larger, and we can be interested in differences between boxes that are less than the external errors. We did not estimate the errors for B,

Table 6. Estimates of the b_σ parameter. The Δ values are the value of b_σ in the row above minus the value in the current row, except for A2kp which we subtract from A.

Name	b_σ (km s^{-1})	error (km s^{-1})	Δ (km s^{-1})
A	26.7	0.2	...
A2	25.6	0.4	1.1
A3	24.8	0.5	0.8
A4	24.1	0.8	0.7
A6	22.4	1.2	1.7
A7
A2kp	26.2	0.4	0.5
A3kp	26.3	0.5	-0.1
A4kp	26.3	0.7	0.0
B2	22.3	0.8	...
B	22.1	0.8	0.2
A4	24.1	0.8	-2.0
B3	28.3	0.8	-4.2

B2 and B3 but we give the value of 0.8 km s^{-1} from A4 because these boxes are all the same size and contain the same number of Ly α lines of a given N_{HI} .

The mode of the b -value distribution is $b_{\text{peak}} = 0.9457b_\sigma$. We do not list b_σ for A7 because this box is barely large enough to contain a single complete line, and we do not obtain fits to b -values. The b -values show a simple trend: a systematic increase with increasing box size, consistent with the change in shape of the pdf of the b -values. We discuss the convergence behaviour of this statistic in §10.

4.2.2 Column Density Distribution: $f(N)$

In Figure 14 we show the distribution of the H I column densities of the lines, relative to the values for box A. Here the function $f(N)$ is the differential distribution of lines, per (linear) cm^{-2} , and per unit absorption distance X . The coordinate $X(z)$ is defined such that the density of absorbers per unit X should be independent of X and z . The number density of non-evolving objects per unit redshift along a line of sight is given by (Tytler 1981, Eqn. 3)

$$N(z) = N_o Y^2 (H(z)/H_o)^{-1} \quad (9)$$

where $Y \equiv (1+z)$ and we define the function

$$\begin{aligned} H(z)/H_o &\equiv E(z) \\ &= [\Omega_M Y^3 + (1 - \Omega_M - \Omega_\Lambda) Y^2 + \Omega_\Lambda]^{1/2} \end{aligned}$$

Setting $X(z=0) = 0$, X can then be defined (Tytler 1982) using $N(X) = N(z) dz/dX = \text{constant}$, which gives

$$\begin{aligned} X(z) &= \int_0^z Y^2 E^{-1}(z) dz \\ &= \int_0^z Y [Y(1+z\Omega_m) - z(2+z)\Omega_\Lambda]^{-1/2} dz \quad (10) \end{aligned}$$

Until this decade it was common to use models with $\Omega_\Lambda = 0$ and $q_0 = 0$ or $1/2$. We now use the cosmological parameters that we gave in §2, $\Omega_\Lambda = 0.73$ and $\Omega_m = 0.27$, which at $z = 2$ give $dX/dz = 3.17801$. For $q_0 = 0$ the value of $dX/dz = 3$ is similar, but for $q_0 = 1/2$ we have the

Table 7. The Column Density Distribution for simulation A. $f(N)$ is lines with line central optical depth $\tau > 10^{-5}$ per cm^{-2} per unit X , the absorption distance from Eqn. 10. The lines are counted in bins of width 0.2 in $\log N_{\text{HI}}$ (e.g. 11.4 – 11.6), and we report the value at the listed bin centres (e.g. 11.5). When we estimate $f(N)$ in bins of width $\log N_{\text{HI}} = 0.5$ instead, we find differences of approximately 0.02 at $\log N_{\text{HI}} \simeq 13 \text{ cm}^{-2}$, and 0.05 at $19 < \log N_{\text{HI}} < 20 \text{ cm}^{-2}$.

$\log N_{\text{HI}}$ (cm^{-2})	$\log f(N)$ ($\text{cm}^2 X^{-1}$)	$\log N_{\text{HI}}$ (cm^{-2})	$\log f(N)$ ($\text{cm}^2 X^{-1}$)
11.5	-9.80489	16.3	-16.9895
11.7	-9.91356	16.5	-17.2893
11.9	-10.0239	16.7	-17.5894
12.1	-10.1645	16.9	-17.9246
12.3	-10.3565	17.1	-18.2563
12.5	-10.5504	17.3	-18.5748
12.7	-10.8223	17.5	-18.9155
12.9	-11.1150	17.7	-19.1734
13.1	-11.4108	17.9	-19.4402
13.3	-11.7170	18.1	-19.7179
13.5	-12.0511	18.3	-20.0306
13.7	-12.3695	18.5	-20.3788
13.9	-12.7416	18.7	-20.7238
14.1	-13.1143	18.9	-21.1386
14.3	-13.4898	19.1	-21.5316
14.5	-13.9236	19.3	-21.8351
14.7	-14.2540	19.5	-22.1258
14.9	-14.6523	19.7	-22.4385
15.1	-15.0434	19.9	-22.7923
15.3	-15.4000	20.1	-23.1537
15.5	-15.7948	20.3	-23.5523
15.7	-16.0774	20.5	-24.0321
15.9	-16.3919	20.7	-24.3957
16.1	-16.7003	20.9	-24.8255

significantly different value $dX/dz = 3^{1/2} = 1.73$. A single sight line through the A box then covers $\delta X = (dX/dz)\delta z = 0.163571$ where $\delta z = L_v(1+z)/c = 0.0514693$ and L_v is the velocity span of one sight line, $5143.37 \text{ km s}^{-1}$.

Larger boxes have larger maximum column densities. The smallest box A7 has no lines with $\log N_{\text{HI}} > 15 \text{ cm}^{-2}$ while the larger boxes have a higher density of lines with $\log N_{\text{HI}} < 17 \text{ cm}^{-2}$. Indeed the trends are rather complex with e.g., box A showing a noticeably higher density of systems with $14.5 < \log N_{\text{HI}} < 16 \text{ cm}^{-2}$ than all the other boxes. We see strong correlations between the $f(N)$ values for similar N values because adjacent sight lines sample almost the same absorbing gas and hence almost the same column densities. We also see large deviations when N_{HI} changes by about a factor of ten. Together these features make it hard to assess the errors and rate of convergence.

In Figure 15 we compare observed values for the column density distribution to the values from box A. We list values for box A in Table 7. We have attempted to correct the data to $z = 2$ and our X definition.

Numerical simulations have often found too few systems with high N_{HI} values (Katz et al. 1996; Gnedin 1998; Gardner et al. 2001; D’Odorico et al. 2006). Simulations need both sufficient volume to contain the long wavelengths modes to get enough CDM halos (Bagla & Ray 2005), and they need high enough resolution to make the clumps of gas that cause Lyman limit systems (LLS). In recent work, Kohler & Gnedin (2007) are able to reproduce both the

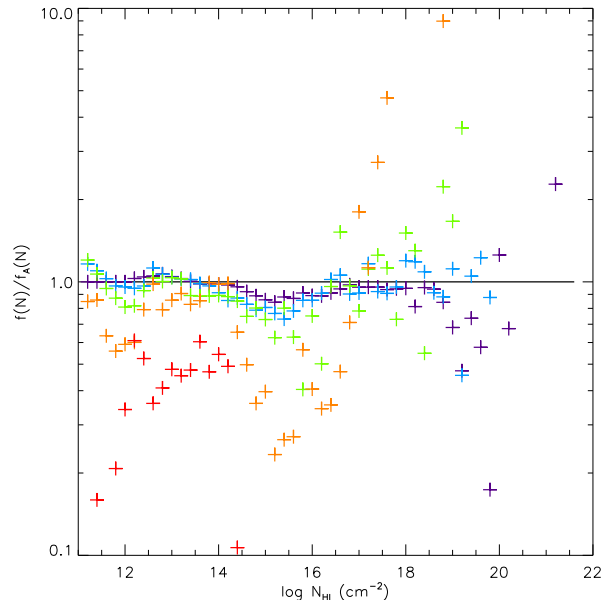


Figure 14. The column density distribution $f(N)$ relative to the A box.

mean flux in the forest and the column density distribution of LLS at $z = 4$ in $4h^{-1}$ Mpc boxes with $2h^{-1}$ kpc resolution. They also obtained approximately the real number of LLS per unit z .

Our simulations lack absorption systems with large column densities. We lack a factor of 1.2 for $14 < \log N_{\text{HI}} < 15 \text{ cm}^{-2}$. We see an increasing lack at $\log N_{\text{HI}} > 17 \text{ cm}^{-2}$, reaching a factor of approximately 30 by $\log N_{\text{HI}} = 19 \text{ cm}^{-2}$, and a factor of 70 for Damped Ly α lines (DLAs) with $\log N_{\text{HI}} \simeq 21 \text{ cm}^{-2}$. The point shown as a plus from Petitjean et al. (1993) is unreliable at $\log N_{\text{HI}} \simeq 19 \text{ cm}^{-2}$. We are also uncertain about the errors in the $f(N)$ measurements, especially since we have not checked that the $f(N)$ values are consistent with the total mean absorption that we assume at $z = 2$. Our simulation A has approximately the correct total absorption, and hence the excess lines with $\log N_{\text{HI}} < 14 \text{ cm}^{-2}$ should make approximately the same total absorption as the lack with $\log N_{\text{HI}} > 14 \text{ cm}^{-2}$.

The lack at the higher columns, $\log N_{\text{HI}} > 17 \text{ cm}^{-2}$ is due to insufficient numerical resolution in collapsed halos which give rise to this absorption and the lack of self-shielding against the UV background radiation. The lack is large enough that we must clearly remove high column lines from both simulations and real spectra when we want to make quantitative comparisons, as first pointed out by Tytler et al. (2004) and Jena et al. (2005).

5 1D POWER SPECTRA OF THE FLUX

Following Croft & Gaztanaga (1997) and others, we define the flux contrast as

$$f(u) = (F/\bar{F}) - 1, \quad (11)$$

where u is velocity and \bar{F} is the mean of the flux from all spectra through a box, listed in Table 5. While our

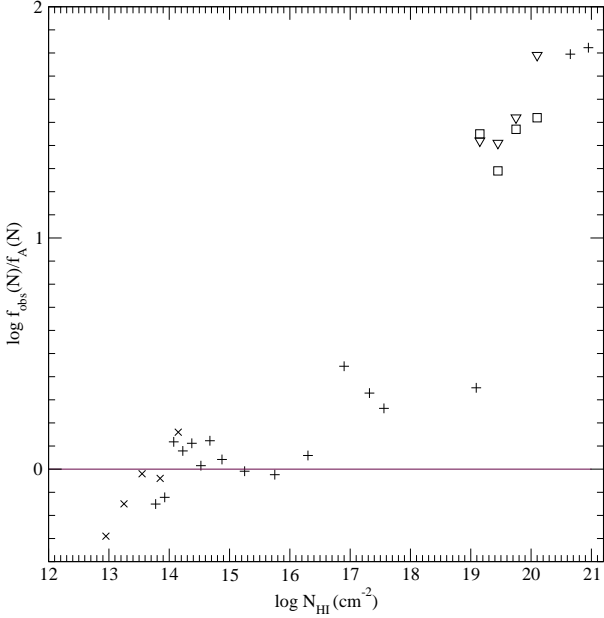


Figure 15. The column density distribution at $z = 2$ from observational data relative to the box A. We use linear interpolation on the $f(N)$ values for box A from Table 7 to find values at the $\log N_{\text{HI}}$ given in data tables. The observations points are from Kim et al. (1997) (x), Petitjean et al. (1993) (+) and O’Meara et al. (2007) (squares: MIKE, triangles: UVES). We make no changes to the $f(N)$ values from O’Meara et al. (2007, Table 5 & Fig. 7) because they use $\Omega_{\Lambda} = 0.7$ while we use 0.73, which is a small difference, and they find no evidence for rapid evolution. If instead, the number of these lines per unit z were to evolve as rapidly as $N(z) \propto (1+z)^{2.6}$ then $f(N, X) \propto (1+z)^{2.1}$ (O’Meara et al. (2007) find that the power drops by approximately 0.5 for $z > 2$ when we change from z to X) and the points drop by 0.23 for MIKE and 0.33 for UVES. We make two types of corrections to all the other points. We define $f(N, X)$ using $X(z)$ and dX/dz as in Eqn. 10 for our assumed cosmology. Both Kim et al. (1997) and Petitjean et al. (1993) use $X_p(z) = 0.5[(1+z)^2 - 1]$ for $\Omega_{\Lambda} = 0$ and $q_0 = 0$ giving $dX_p/dz = (1+z)$. We calculate $f(N, X) = f(N, X_p)(dX_p/dz)/(dX/dz)$, at the mean redshift of each sample, where $f(N, X_p)$ are the published values. For Kim et al. (1997) we take the $f(N, X_p)$ values from Table 2, with a mean $z = 2.31$ from two QSOs, and we multiply these values by a factor $d(X_p)/dX = 0.980$. For Petitjean et al. (1993) we take the $f(N, X_p)$ values from Table 2. We assume a mean $z = 2.8$, the mean z_{em} from Table 1, weighted by the number of lines and evaluated for Ly α at a rest wavelength of 1120 Å. We multiply these $f(N, X_p)$ values by a factor $d(X_p)/dX = 1.037$. For $\log N_{\text{HI}} < 17.2 \text{ cm}^{-2}$ we make corrections for redshift evolution assuming $f(N)$ per unit z evolves as $N(z) \propto (1+z)^{2.8}$ (Kirkman et al. 2005, 2007), and hence $f(N, X) \propto (1+z)^{2.3}$. We then multiply the $f(N, X)$ values from Kim et al. (1997) by 0.798 and those from Petitjean et al. (1993) by 0.581. For $17.2 < \log N_{\text{HI}} < 19.1 \text{ cm}^{-2}$ we assume that the $N(z) \propto (1+z)^{2.8}$ (Sargent et al. 1989; Lanzetta 1991; Stengler-Larrea et al. 1995) and a mean redshift of 3.0. These evolution correction factors could have large errors. The point from Petitjean et al. (1993) at $\log N_{\text{HI}} 19.09 \text{ cm}^{-2}$ is for a large range for $17.68 < \log N_{\text{HI}} < 20.5 \text{ cm}^{-2}$. We plot the point at the mean of the , but lower $\log N_{\text{HI}}$ lines tend to be more common, so the point should be plotted at some (unknown) lower N_{HI} value.

signal looks like that used by Croft et al. (1998) and McDonald et al. (2000), there is an important difference. They both take \bar{F} to be the mean flux in each spectrum. We discuss this alternative choice below in §8.

Since the mode of the flux in each pixel is larger than the mean flux, $f(u)$ is typically larger than zero. This definition resembles that of $\delta_{\text{CDM}-1}$, except that δ_{CDM} involves division by the mean density of CDM that is a parameter input into the simulations and identical for all. In contrast, the mean flux is not known until spectra are made, and it varies from simulation to simulation and with z .

We compute the Fourier transform of the flux contrast using $f(u)$ in place of $\delta_{\text{CDM}-1}$ in Eqn. 5. We measure the (one-dimensional) flux power of each sight line in the z direction, and we present the average of the power from all sight lines. We have explicitly checked that we obtain the same power as does McDonald from the same spectrum.

In Figure 16 we show the power spectrum of the flux, P_F , in this case from all spectra parallel to the z axis in each simulation. We tabulate values in Tables 8 and 9, and in Figure 17 we show the power divided by that in simulation A. In contrast to the CDM power, the differences between simulations are small, and of the opposite sign. In general, the larger boxes have smaller flux power, the opposite of the trend that we saw in Fig. 5 for the power of the CDM. On the largest scale sampled by a box, the power at $\log k < -2 \text{ s/km}$ in the A2 and A3 boxes is slightly less than that in the largest A box. This might be simply the effect of the larger modes in the larger boxes. On intermediate scales $-1.5 < \log k < -0.6$ there is a systematic decrease in power with increasing box size, with larger changes on smaller scales (larger k). However, on the smallest scales, $\log k > -0.5 \text{ s/km}$, corresponding to sine wavelengths $\lambda < 20 \text{ km s}^{-1}$ (4 cells in the simulation), the trends change direction. The differences between the simulations become less, and A2 returns to approximately the same power as A. The largest deviations in the ratios of the power of the flux are seen at $\log k > -0.7 \text{ (s/km)}$, corresponding to changes in the shapes of the narrow lines.

The large changes in the power of the CDM with box size, contrasted with the small changes in the power of the flux implies that the bias will change rapidly with box size, approximately as does the CDM. Attention must be given to the appropriate smoothing of the fields to reduce the sensitivity of the CDM power to the box size (McDonald et al. 2002).

McDonald (2003) shows how the power of the flux changes when he increases his box size from 28.2 to 56.3 to 112.7 Mpc, while keeping the cell size constant at 220 kpc. He also sees that the power is lower in the smaller boxes

We see that the change in power with box-size is consistent with the simultaneous change in the b -value distribution. Viel et al. (2003) showed quantitatively how power of the flux on small scales responds to changes in line b -values. For $-2 < \log k < -0.2$ Viel et al. (2003) saw essentially the same power from randomly placed Ly α lines as from real spectra. They also showed that making all b -values larger by a factor of two decreased the power at $-1.5 < \log k < -0.7$. Our larger boxes have larger b -values and they show decreased power on these scales. If all other factors are unchanged, we would expect higher temperatures for the IGM in larger boxes, which we confirm in §6.2.

Table 8. The log of the power of the flux in the A series simulations. The subscripts are values of $\log(k)$ (s/km), and the R are the ratios of the power (not the log) to the values in A at the same k .

Box	$\log P_{-2.5}$	$\log P_{-2}$	$\log P_{-1.5}$	$\log P_{-1}$	$R_{-2.5}$	R_{-2}	$R_{-1.5}$	R_{-1}
A	0.933	0.757	0.239	-1.310	1.00	1.00	1.00	1.00
A2	0.910	0.739	0.246	-1.279	0.95	0.96	1.02	1.08
A3	0.767	0.253	-1.233	1.02	1.03	1.20
A4	0.742	0.325	-1.144	0.97	1.22	1.47
A6	0.336	-1.060	1.25	1.78
A7	-0.945	2.32
A2KP	0.919	0.747	0.244	-1.325	0.97	0.98	1.01	0.97
A3KP	0.784	0.255	-1.314	1.07	1.04	0.99
A4KP	0.778	0.342	-1.238	1.05	1.27	1.18

Table 9. The 1D power spectrum of the flux in simulation A. We include all wavenumbers below $k \leq 0.01$ (s/km). We then pick eight points from each $\log k$ decade and we force the last point to be the Nyquist frequency. We computed the error on the power from 4x4 tiles across the face of the box. The error is the standard error on the mean power from all the tiles. The P_e and its error refer to the evolving spectra that we discuss in §B. We shows power of ten in parenthesis: $3.522(-8) = 3.522 \times 10^{-8}$.

$\log k$	$P(k)$	$P_e(k)$ (km/s)	error	error _e
-2.9134	10.016	10.021	0.441	0.441
-2.6124	9.371	9.377	0.409	0.411
-2.4363	8.134	8.135	0.381	0.382
-2.3114	7.576	7.576	0.363	0.364
-2.2144	6.865	6.872	0.311	0.311
-2.1353	6.446	6.447	0.283	0.284
-2.0683	6.053	6.057	0.270	0.270
-2.0103	5.790	5.794	0.250	0.251
-1.9592	5.407	5.412	0.236	0.237
-1.6830	3.264	3.260	0.124	0.123
-1.5155	1.855	1.849	0.651(-1)	0.648(-1)
-1.3949	1.068	1.068	0.315(-1)	0.314(-1)
-1.3006	6.243(-1)	6.256(-1)	0.170(-1)	0.171(-1)
-1.2232	3.748(-1)	3.749(-1)	0.106(-1)	0.107(-1)
-1.1575	2.269(-1)	2.273(-1)	0.600(-2)	0.620(-2)
-1.1005	1.376(-1)	1.376(-1)	0.375(-2)	0.380(-2)
-1.0501	8.435(-2)	8.398(-2)	0.226(-2)	0.229(-2)
-1.0049	5.185(-2)	5.171(-2)	0.149(-2)	0.149(-2)
-0.8565	7.716(-3)	7.725(-3)	0.266(-3)	0.272(-3)
-0.6630	2.878(-4)	2.904(-4)	0.137(-4)	0.140(-4)
-0.5296	2.210(-5)	2.215(-5)	0.121(-5)	0.127(-5)
-0.4277	3.272(-6)	3.633(-6)	0.196(-6)	0.269(-6)
-0.3452	7.803(-7)	9.018(-7)	0.451(-7)	0.954(-7)
-0.2759	2.357(-7)	3.350(-7)	1.341(-8)	5.048(-8)
-0.2162	1.296(-7)	2.193(-7)	7.166(-9)	3.727(-8)
-0.2041	1.286(-7)	2.073(-7)	7.110(-9)	3.522(-8)

5.1 Autocorrelation of the Flux

Although containing exactly the same information as the power, the autocorrelation can better illustrate characteristics of the signal that are hard to see in the power, such as correlations over large scales. While a power spectrum is a complete statistical description of a random Gaussian field, the flux distribution is far from Gaussian, hence neither the power spectrum nor the autocorrelation will be a complete description.

The autocorrelation of the flux for a given velocity shift δu can be computed directly from a transmission spectrum as $\xi_F(\delta u) = \langle (F(u) - \bar{F})(F(u + \delta u) - \bar{F}) \rangle$, where \bar{F} is

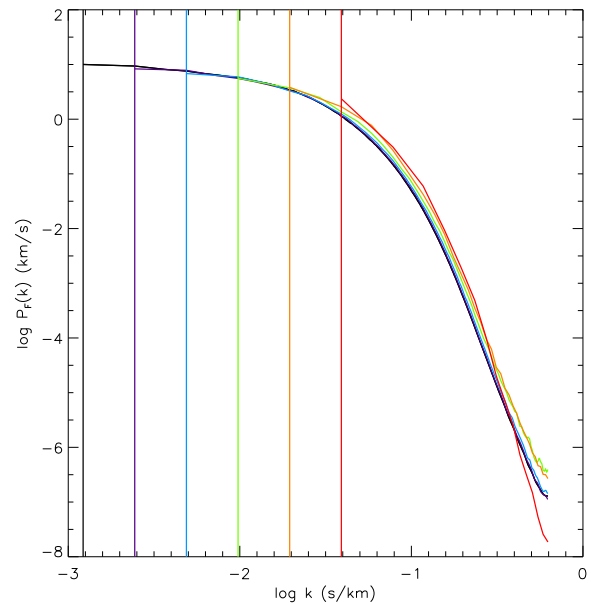


Figure 16. The power spectrum of the 1D flux contrast (Eqn. 11, flux divided by mean flux in that simulation box) from A-series boxes for all N^2 sight lines along the z-direction. The k is in s/km and the smallest boxes gives the smallest amount of power at $\log k = -1$.

the mean flux in a box from Table 5. The brackets refer to an average across the pixels of the spectrum. We choose to obtain the autocorrelation from

$$\xi_F(\delta u) = \frac{\bar{F}^2}{2\pi} \int P(k) e^{jk\delta u} dk \quad (12)$$

where $P(k)$ is the power of the flux contrast and we can use the line of sight averaged power directly because we have divided by the mean flux of each cube. The results we report here, as with the flux power, are the average autocorrelation profiles at each velocity shift from all lines of sight.

For the power spectrum, the longest non-zero mode is one wave in the box. By analogy, for a sight line parallel to the box edges, the largest lag in a box is $u = L_v/2$. We expect the autocorrelation to decrease up to scales of $L_v/2$ and then to rise again, since a lag of u in one direction is simultaneously a lag of $L_v - u$ in the reverse direction. This is in contrast with real spectra where the autocorrelation will continue to decrease with increasing lag. The number

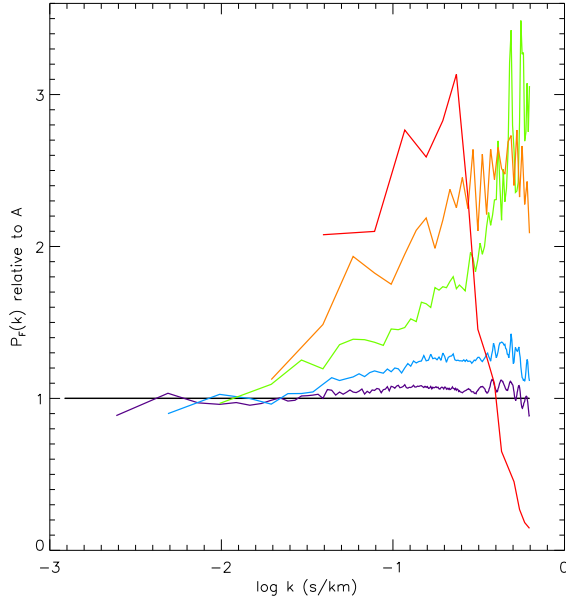


Figure 17. The power spectrum as in Fig. 16 but now divided by the power from simulation A, which is the line at vertical value 1.

of samples of each lag drops from N for lags of one pixel to $N/2$ for lags of $L/2$. When we shift a spectrum by some lag, we loop around the periodic boundary conditions, making the first and last pixels adjacent, so that all shifted spectra have the same length.

In Figure 18 we show the autocorrelation of the flux calculated using the mean of the flux from all spectra through each box. The autocorrelation of the flux falls with increasing lags, and it falls to lower values in larger boxes. The larger boxes also have smaller correlation for most velocity lags. However, the autocorrelation does not drop to zero on the largest scales in a box, rather it stops falling at some low plateau value.

If we define the autocorrelation using the mean flux in each sight line \bar{F}_L , instead of the mean of the box, then the autocorrelations are all reduced. We show these autocorrelation functions as dashed lines in Fig. 18. The amount by which the two autocorrelation calculations differ is equal to the variance of the line of sight mean flux values about their mean, which is the mean flux of each cube that we give in Table 5,

$$\Delta\xi_F(\delta u) = \frac{1}{N^2} \sum_{L=1}^{N^2} (\bar{F} - \bar{F}_L)^2 \equiv \text{Var}(\bar{F}_L), \quad (13)$$

where N^2 is the number of sight lines we use to sample each N^3 box. The smaller boxes have larger sight-line to sight-line variance, as can be seen in Fig. 19 and hence their autocorrelation (and other statistics) is decreased the most then we use the mean flux per sight line.

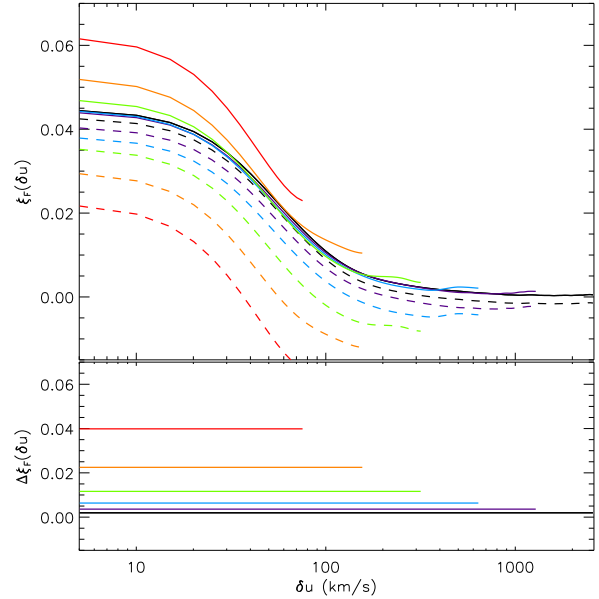


Figure 18. How the autocorrelation of the flux depends on box size and the definition of the signal. Autocorrelation vertically against velocity lag horizontally. The solid curves were calculated using the mean flux of the box. The dotted curves use instead the mean flux of each sight line, \bar{F}_L . We show the difference of the two, from Eqn. 13, in the bottom panel. The signals from the larger boxes extend farthest to the right.

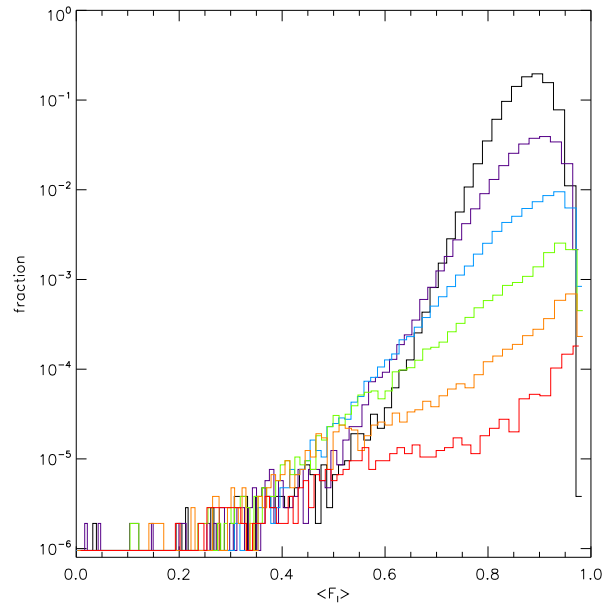


Figure 19. The distribution of the mean flux per sight line, \bar{F}_L , for all simulations in the A series. The vertical scale shows the number of sight lines, divided by the number of sight lines in the A box. This division lowers the distributions from the smaller boxes (lower histograms at $F_L = 0.8$) making it easier to see each distribution.

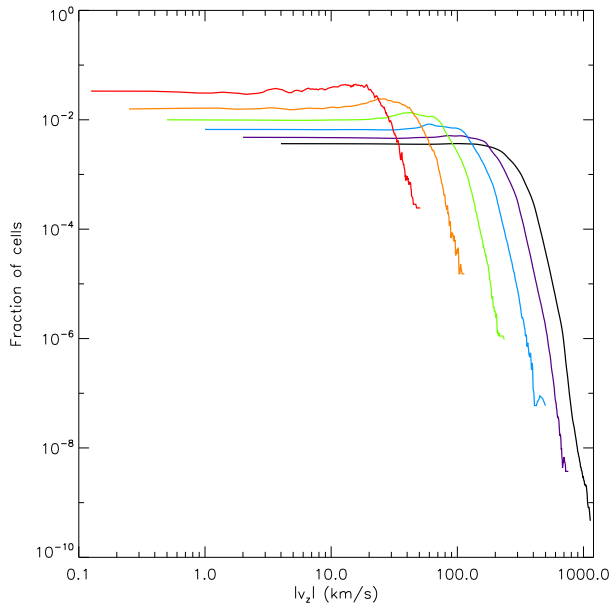


Figure 20. The change in the velocity field with box size. The fraction of cells, on a log scale, as a function of the modulus of the gas velocity in the z direction. We sample the fractions in steps of 8 km s^{-1} for A 4 km s^{-1} for A2, 2 km s^{-1} for A3, 1 km s^{-1} for A4, 0.5 km s^{-1} A6 and 0.25 km s^{-1} for A7, and we report the fraction of cells per 1 km s^{-1} , for all simulations, which accounts for why the total area under the curves falls with increasing box size.

6 VELOCITY FIELD, BARYON TEMPERATURE AND BARYON DENSITY

Having seen how the statistical properties of the Ly α forest depend on box size we now return to examine the changes in the velocity field, and the baryon temperature and baryon density in the simulations, since these fields control how the Ly α forest changes.

6.1 How gas velocity changes with box size

In Fig. 20 we see that the velocity of the cells increases dramatically with increasing box size. Velocities $> 160 \text{ km s}^{-1}$ are common in the three largest boxes but non-existent in the two smallest boxes. In Table 10 we list the minimum, median and maximum baryon velocity in each box. These velocities increase by factors of 1.23 – 2.59 as we double the box size, with the largest factors applying to the maximum velocity for the smallest pair of boxes. The maximum changes the most because this is sensitive to the rare high density regions. However, all cells show a systematic increase in velocity, as illustrated by the factor of 1.34 increase in the median velocity going from the A2 to A box.

6.2 How gas temperature and density change with box size

In Tytler et al. (2004, Fig. 19) we showed the temperature of cells in simulation B as a function of their baryon density. Simulation B has the same parameters as the A series used here, but with cells that are half the size. We fit a broken

Table 10. Statistics of the proper velocity (km/s) for the baryons in the cells in the A series simulations.

Box	mean	median	max
A	136.4	138.2	1153.9
A2	110.8	103.0	764.3
A3	74.9	70.9	515.1
A4	47.2	45.0	277.2
A6	27.8	26.7	153.3
A7	14.1	13.8	59.2

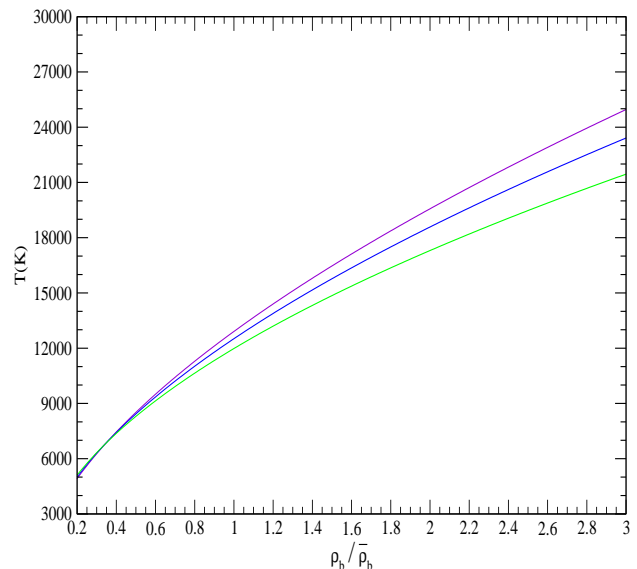


Figure 21. Power law fits to the most common temperature at a given baryon overdensity, from J05 Table 9. The fits shown, from top to bottom on the right, are for the A2, A3 and A4 simulations.

power law to the ridge line that specifies the most common T at a given density, but noted that these fits were not very satisfactory in shape. In Table 9 of J05 we fit single power laws $T(\rho) = T_0(\rho_b/\bar{\rho}_b)^\alpha$ to $0.2 < \rho_b/\bar{\rho}_b < 3$ in many simulations, where $\bar{\rho}_b$ is the cosmological density of baryons. We found values of $T_0 = 11,982, 12,561$ and $12,910 \text{ K}$ for A4, A3 and A2, showing an increase in temperature at a given density with box size. We also saw a systematic increase in the index α with box size which corresponds to a larger difference in temperature at higher densities, and near identical temperatures at $\rho_b/\bar{\rho}_b = 0.35$. In Figure 21 we show these fits for simulations A4, A3 and A2.

Fig. 22 is a contour plot of the temperature T of cells as a function of baryon overdensity for simulations A and A4. The vertical axis is $T/(\rho_b/\bar{\rho}_b)^{0.5}$ to remove much of the tendency for T to increase with density. We are most interested in the densities that produce the Ly α forest. We found in §3 that Schaye (2001, Eqn. 10) suggests that the Ly α forest lines with $\log N_{\text{HI}} = 12.5 - 14.5 \text{ cm}^{-2}$ that we use to study the b -value distribution typically come from baryon

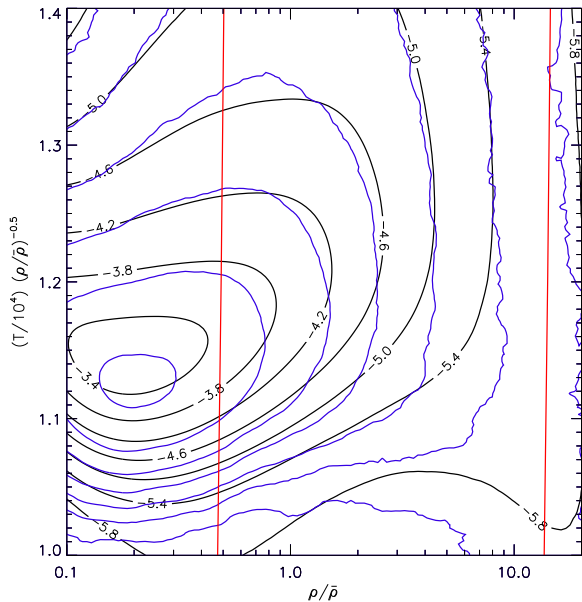


Figure 22. Contour plot of the temperature of cells against their baryon overdensity. Blue and black contours correspond to A4 and A boxes respectively. We generate the contours from the scatter plot between the grid values of $T/(\rho_b/\bar{\rho}_b)^{0.5}$ and $\rho_b/\bar{\rho}_b$ by binning the x-axis and y-axis in logarithmic intervals of 0.001 and 0.02 respectively and computing the number of points in each 2D mesh. The iso-level values show the fraction of points (in logarithmic units) contained within each contour relative to the total number of points in the simulation contained within the boundaries of each axis. The nearly vertical line on the left shows the typical cells responsible for Ly α lines with $\log N_{\text{HI}} = 12.5 \text{ cm}^{-2}$ while the line on the right is for 14.5 cm^{-2} .

overdensities 0.5 – 15.7. On Fig. 22 we show lines of constant $\log N_{\text{HI}}$,

$$T = 10^4 K \left(\frac{8.82 \times 10^{12}}{N_{\text{HI}} \text{ cm}^{-2}} \right)^{3.846} \left(\frac{\rho}{\bar{\rho}} \right)^{5.769}, \quad (14)$$

obtained from Schaye (2001, Eqn. 10). We see, with close inspection, that, at overdensities above $\simeq 0.5$ the contours of the larger box have on average shifted to higher temperatures, particularly in the regions closer to the frequency peak of this 2D distribution. The gas that makes the Ly α forest absorption is clearly hotter in the larger box.

In Fig. 23 we show the pdf of the temperature per cell for three different baryon overdensity ranges, 0.5 – 1.5, 1.5 – 5 and 5 – 15. For each density range, we show six distributions, one for each box size. The temperature pdf shows very little change with box size for low overdensities 0.5 – 1.5, but the intermediate and especially the higher densities the larger boxes have systematically higher temperatures. This tendency of increasing temperature with box size at higher but not lower overdensities confirms the power law fits to the most common temperatures from J05 that we showed in Fig. 21.

In Fig. 24 we show the mean temperature of cells as a function of baryon overdensity for the A series simulations. We see a dramatic increase in the mean temperature in the larger boxes especially at higher overdensities. The percentage increase in the mean temperature with box size

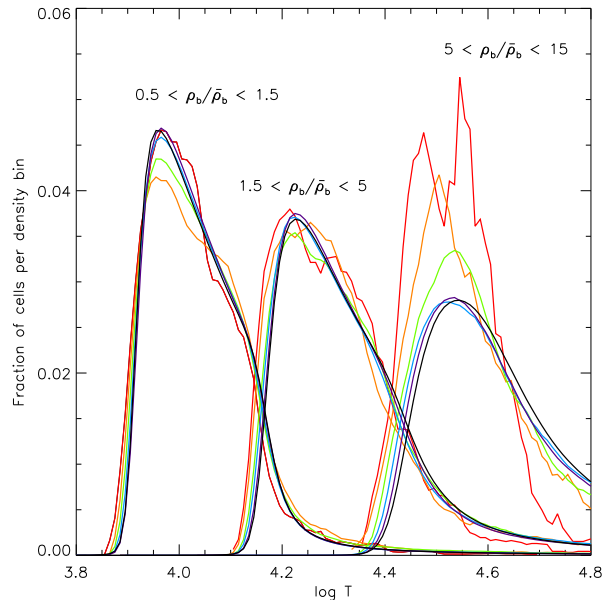


Figure 23. The pdf of the temperature (in K) of cells for three contiguous ranges of baryon overdensity, the ranges that are responsible for Ly α lines with $\log N_{\text{HI}} > 12.5 \text{ cm}^{-2}$ (the histograms on the left for the lower overdensities) to $< 14.5 \text{ cm}^{-2}$ (histograms on the right for the higher overdensities). We show the fraction of all cells in the density range, and we sample the temperature in steps of $\log T = 0.01$.

decreases at lower overdensities, as we just saw for the much more restricted range of densities in 23.

Fig. 25 is like Fig. 24 but now showing the temperature which is exceeded by 50% of cells, the median. We again see that the larger boxes are hotter but the differences are much smaller, especially at the low densities of the Ly α forest. The much larger increase in the mean temperature comes from relatively few cells that have undergone shock heating to temperatures much larger than the median and well above the temperature at which there is sufficient H I to make Ly α lines.

In Fig. 26 we see that relatively few cells are attaining much higher temperatures in the larger boxes. The temperatures above 10^5 K come from shocks which are rarer and weaker in the smaller boxes because the velocities and peak densities are lower.

Fig. 27 summarizes the changes in temperature with box size, and shows that the trends of relevance to the Ly α forest are only revealed by specific statistical measures.

In Fig. 28 we show a slice of the A box one cell thick. We added two contours one of which shows the minimum typical over density for the IGM and the other the upper overdensity. The arrows show the velocity of the cells. While most cells making Ly α absorption are surrounded by cooler gas, those that are flowing into the highest density regions are next to hotter gas.

In Figs. 29 and 30 we show the pdf of the baryon density per cell for different box size. We see that most of the pdf moves to lower density in the larger boxes. In the density range responsible for typical Ly α forest lines with $\log N_{\text{HI}} 12.5 - 14.5 \text{ cm}^{-2}$ there are systematically fewer cells in the

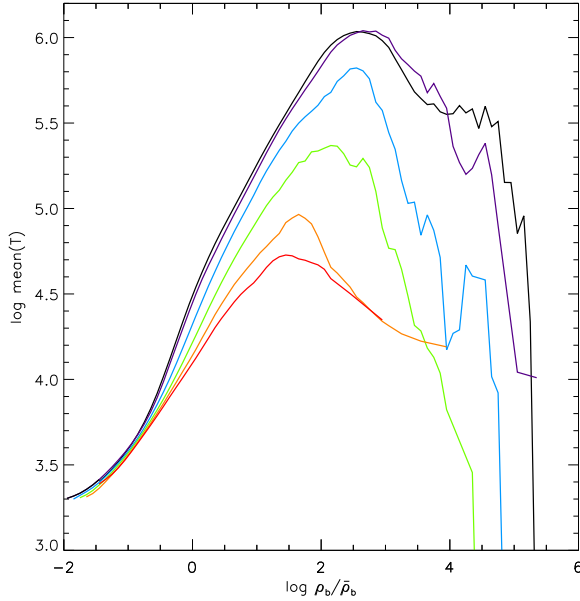


Figure 24. The mean temperature (K) of all cells as a function of log baryon overdensity, evaluated in log overdensity intervals of 0.1. At $-0.5 < \log \rho_b / \bar{\rho}_b < 2.5$ the order of the curves is that of increasing box size towards the top.

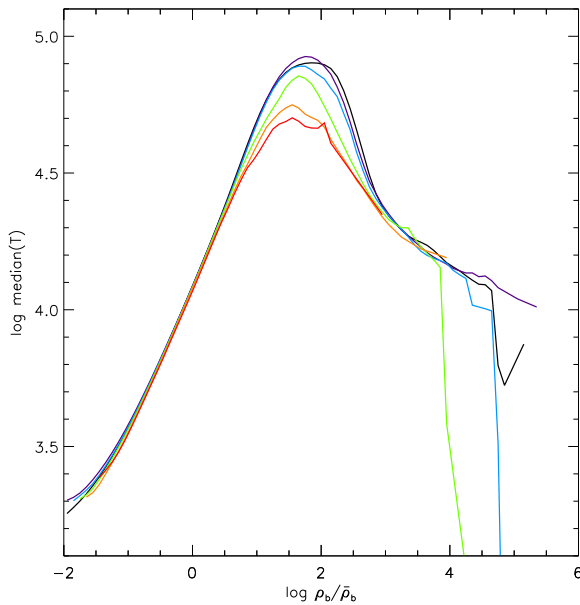


Figure 25. The median temperature (50% are hotter) of all cells as a function of log baryon overdensity, sampled in bins of log overdensity = 0.1. The order of the curves is that of increasing box size to the top at $\log \rho_b / \bar{\rho}_b = 2.2$.

larger boxes, which can explain why we saw in Table 5 less absorption in the larger boxes. If the density distribution drops by a constant factor for all densities relevant to the Ly α forest, then the $f(N)$ will remain unchanged in shape. The log vertical scale in Fig. 30 shows that this is approximately true, but in detail there is a slightly larger rela-

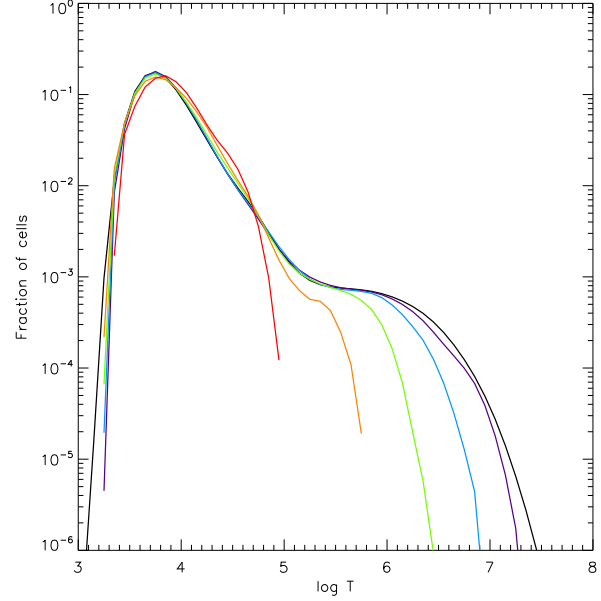


Figure 26. The fraction of cells as a function of baryon temperature (K), sampled in bins of $\log T = 0.1$. The larger boxes extend farther to the right.

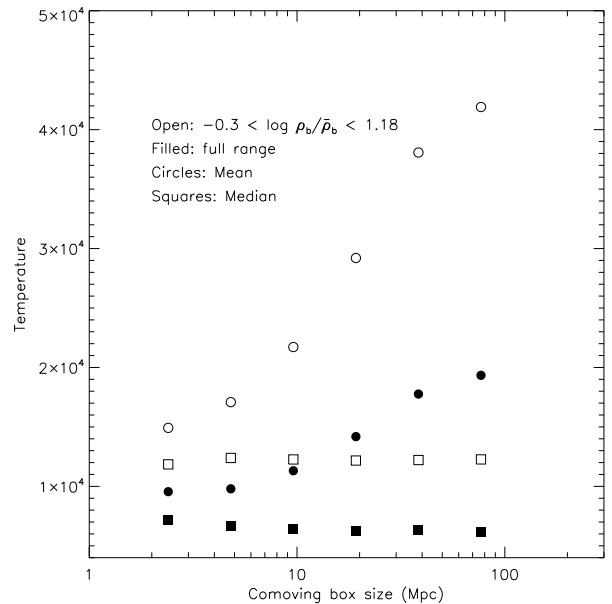


Figure 27. The mean (circles) and median (squares) baryon temperature (K) as a function of box size. We evaluate these statistics in bins of 0.1 in $\log T$, for both the entire box, and for the densities that produce the Ly α forest.

tive decrease in the number of low density cells. The larger boxes then have relatively more lines with higher $\log N_{\text{HI}}$ values, as we have already seen in Fig. 14 for columns $13 < \log N_{\text{HI}} < 15 \text{ cm}^{-2}$. Since lines with higher N_{HI} values tend to be wider, since they come from higher densities where the gas is hotter, consistent with the larger b_σ values in the larger boxes.

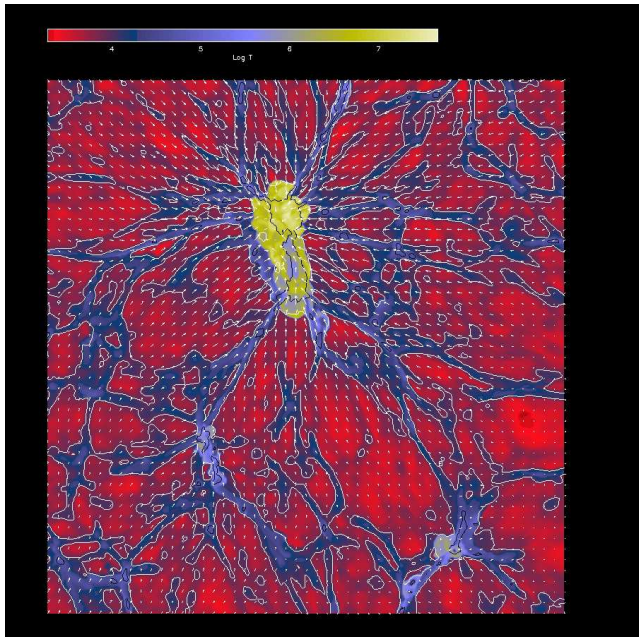


Figure 28. A 30x30 Mpc section of the A box, one cell thick and containing the highest density cell in the whole box. The colour scale shows the baryon temperature, with the red to blue boundary at the typical temperature for a Ly α lines with $\log N_{\text{HI}} = 12.5 \text{ cm}^{-2}$. The red regions are cooler and the yellow and whitish regions are hotter than the blue regions. We show two contours, one for the baryon overdensity of 0.5 and the other for 15, the range responsible for many Ly α forest lines. The arrows show the baryon velocity with a length linearly proportional to the amplitude of the velocity. The typical arrow in the upper right is 280 km s^{-1} .

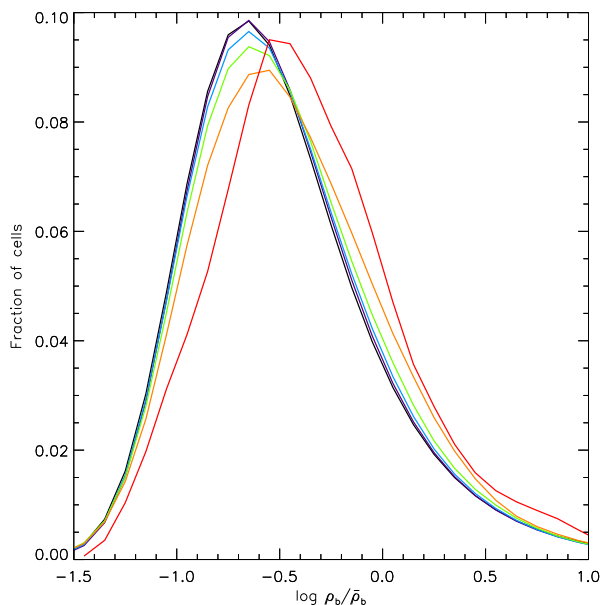


Figure 29. The effect of box size on the pdf of the log baryon overdensity in each cell. At $\log \rho_b / \bar{\rho}_b = 0$ the curves for larger boxes are lower on the plot. The Ly α forest typically comes from $-0.3 < \log \rho_b / \bar{\rho}_b < 1.2$, all to the right of the peak, where the larger boxes have systematically lower fractions of their cells.

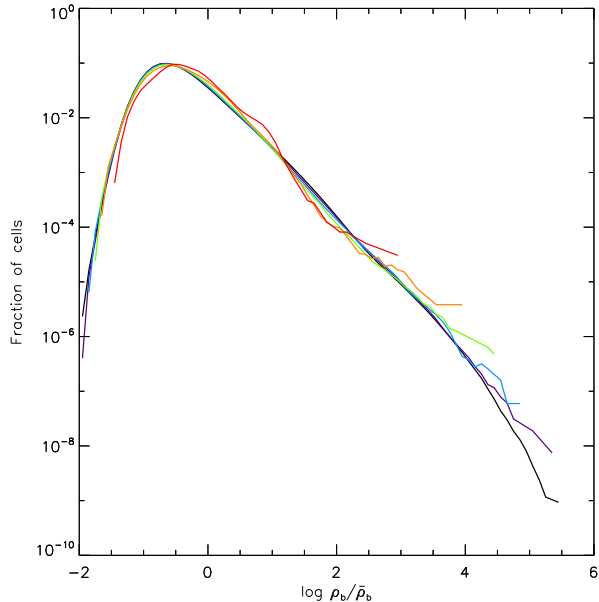


Figure 30. As Fig. 29 but with the log of the fraction of cells on the vertical axis to show the relative changes. The curves for larger boxes extend farther to the right and are lower on the plot at $\rho_b / \bar{\rho}_b = 0$.

7 SIMULATIONS WITH NEARLY CONSTANT MEAN FLUX AND B-VALUES

We ran a second series of simulations using input parameters that we adjusted to make the mean flux and b_σ values approximately constant, at the values for the simulation A. We adjusted the intensity of the UVB γ_{912} and the amount of heating per He II ionization, X_{228} . We determined these parameters iteratively using scaling relations similar to those described in J05. At redshift $z = 2$ the ionizing background were multiplied by the factors γ_{912} , listed in Table 1. For these KP simulations, we also augmented the UVB by additional factors to make the mean flux at those redshifts closer to the values reported in Keck HIRES spectra by Kirkman et al. (2005). At $z \leq 2$ we multiplied the fluxes by 1. At $z = 2 - 3$ we multiply by $1.3(z - 2)$, and at $z > 3$ we multiplied by 1.3.

In Table 5 we see that the mean fluxes are indeed similar to that of A, although the modes are less so. In Table 6 we see that the b_σ values are all similar and between those for A and A2. We could have iterated further to improve the agreement, but felt that this was not necessary for this work.

In Fig. 31 we show the b-value distribution for the KP series. The three are more similar to each other and to A than were the similar sized simulations from the A series, as we expect.

In Fig. 32 we show for the power of the flux contrast for the KP simulations, and in Fig. 33 we show the same divided by the power from A. Comparing to Fig. 17 we see that the power in the KP series is factors of 2 – 3 closer to the power in A than were the simulations of the same size in the A series, though the differences are less reduced on the smallest scales.

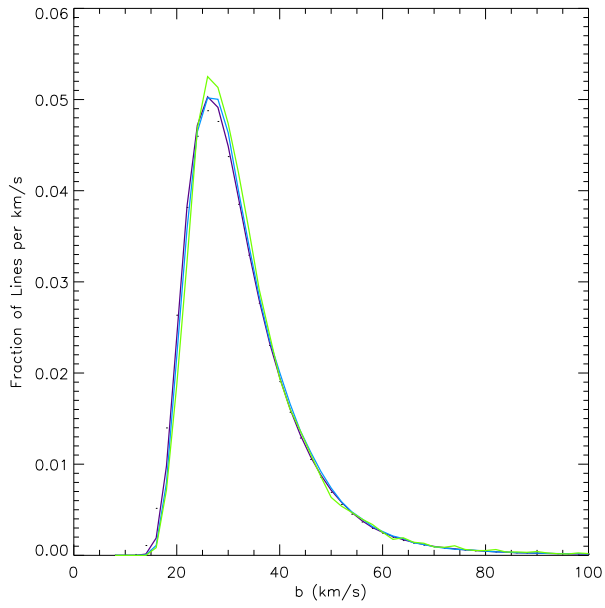


Figure 31. The b -value distribution for boxes in the KP-series, which should be compared to Fig. 12 for the A series simulations. Just to the right of the peak, the curves are from the top A4kp (green), A3kp (blue) and A2kp (violet).

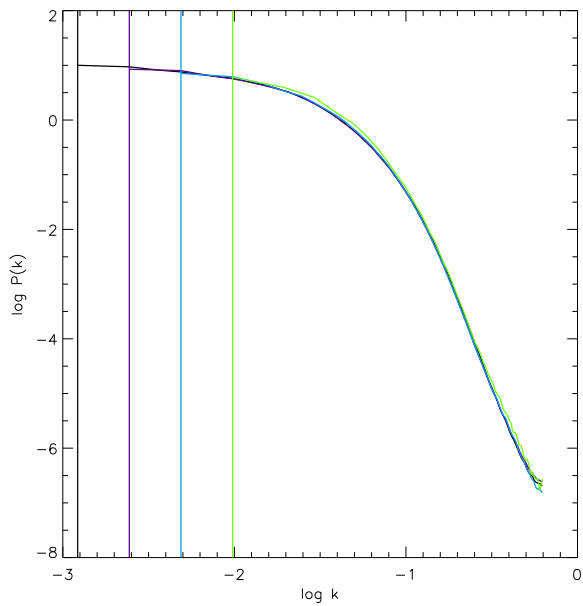


Figure 32. The power spectrum of the 1D flux contrast (Eqn. 11) from KP series, A2kp violet), A3kp (blue) and A4kp (green) together with A (black). The curves from the larger boxes extend farther to the left. Compare to Fig. 16 for the entire A series.

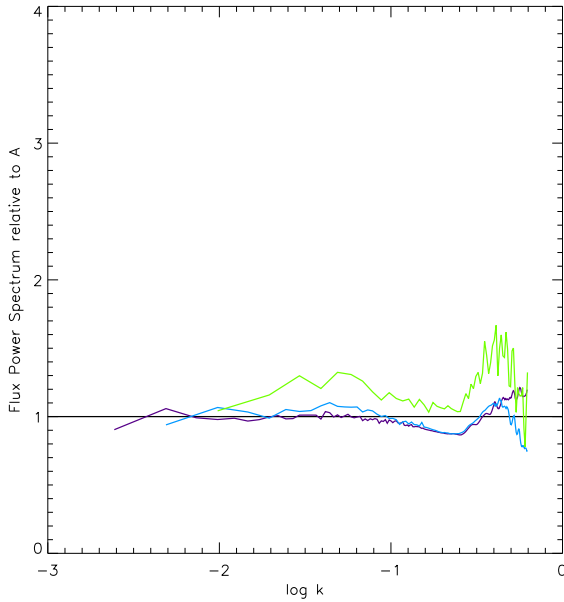


Figure 33. The power spectrum of the 1D flux contrast (Eqn. 11) from KP series divided by the power from A. From bottom to top at $\log k = -0.5$ s/km we show A2kp (violet), A3kp (blue) and A4kp (green). Compare to Fig. 17 which is on nearly the same vertical scale.

In Fig. 34 we see that the distribution of the flux in the KP series is significantly closer to A than are the A series simulation of the same size. The difference is about a factor of two for A3 and A4, such that A4KP is similar to A3, and A3KP is similar to A2. The improvement seems larger for the larger boxes. For A2 the frequency of $Flux = 0.8$ is 1.05 times the frequency in A, while for A2KP this is 1.02. There are even larger improvements at fluxes above 0.97.

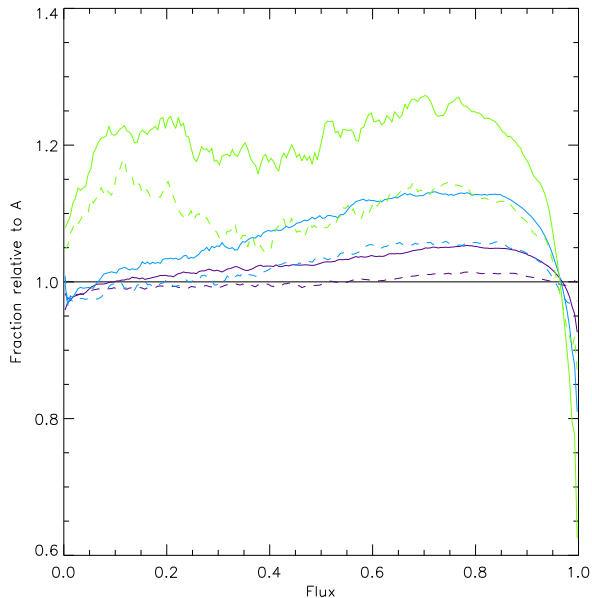


Figure 34. Distribution of the flux per pixel for KP and A series. We show the fraction of pixels divided by those for simulation A. We show simulations A2, A3 and A4 (solid lines) from top to bottom at Flux = 0.7, and below, A2kp, A3kp and A4kp (dashed lines). Compare to Fig. 11 for the A series.

In general, we see that the adjustments in the γ_{912} and X_{228} that we made for the KP series allow a given KP simulations to have approximately Ly α forest statistics of an A series simulation that is twice the size. For some applications, we can then save a factor of 8 in computing resources. We can use larger X_{228} values, corresponding to more heat input, to partially compensate for the effects of limited box size. We simultaneously need smaller γ_{912} values to maintain the same mean flux.

8 SIGNAL DEFINITION AND NORMALISATION

The division by the mean flux can introduce significant ambiguity, because there are many ways to select the mean, and the mean is a function of z . There are two main ways of defining the mean flux; global and local.

In this paper we use global definitions for the mean flux that come close to approximating the true mean flux at each z . We have divided spectra by the mean flux from the whole of each simulation box. We could alternatively have taken an estimate of the mean flux from a calibrated measurement (Tytler et al. 2004; Kirkman et al. 2005, 2007). When we use real spectra we must remove the metal lines and the strong Ly α lines of LLS and DLAs because they add significant absorption to the Ly α forest that is not from the low density IGM and that will be missing from simulations.

In contrast, Hui et al. (2001); Kim et al. (2004b); McDonald et al. (2006) and others have used local measures of the mean flux. They divide each spectrum by its own mean flux, since their goal is to avoid continuum fitting or to reduce the errors in the continuum level. Kim et al. (2004b)

[Fig. 2] obtained similar power spectra at $k > 0.002$ s/km when they divided real spectra by either fitted continua or the mean flux.

We do not advocate division by the local mean flux for several reasons. We need to know the lengths of each spectrum to make a precise comparison with other data or simulations. For extremely long artificial spectra, division by the mean flux in individual spectra is not very different to dividing by the overall mean flux of the whole sample of many spectra, but for the short spectra, including those from our boxes, the differences are huge.

In real spectra the mean flux varies significantly from spectrum to spectrum due to large scale structure. In Tytler et al. (2004) (Fig. 13, 16, Table 4) and we found that at $z = 1.9$ the standard deviation of the mean absorption in 121 Å segments from the low density IGM alone is about 1/3 of the mean amount of absorption. In addition, the metal lines and strong Ly α lines and the low density IGM all contribute similar amounts to the variation in the total amount of absorption. Hence, when we divide by the mean flux in each spectrum, we are removing much of the large scale structure signal, and introducing undesired correlations with the metal lines and strong Ly α lines, with no guarantee that we are removing any errors in the continuum level. Indeed, the continuum level errors of most interest are on the short scales of the flux calibration errors and the emission line shapes, and not necessarily correlated with the mean flux across the whole of a spectrum.

In Figure 35 we show the power spectra of the flux obtained when we divide the flux in each spectrum by the mean flux of that spectrum, P_F^L . We show in Fig. 36 the power of the flux, divided by the mean flux in a sight line, and then divided by the same quantity for box A. The power in the larger boxes is little changed from in Fig. 16 where we divided by the mean flux in the whole box, but the power in the smaller boxes is raised.

9 HOW RESOLUTION CHANGES THE SIMULATED IGM

In Figs. 37 and 38 we show how the pdf of the baryon overdensity per cell varies with the cell size. For the common densities shown in Fig. 37 we see that simulations with smaller cells have systematically lower densities. These changes are larger for cell sizes 150 to 75 to 37.5 kpc, but the changes are too small to see when the cell size drops from 37.5 to 18.75 kpc. The explanation for this trend to lower densities is given in Fig. 38 where we see that simulations with smaller cells contain a few cells with much larger densities. These cells contain the baryons that is depleted from the bulk of the volume.

In Fig. 39 we see the mean temperature of cells at a given baryon overdensity increases with decreasing cell size. The increase is minimal when we decrease the cells from 37.5 to 18.5 kpc, suggesting that 37.5 kpc is small enough for the current work.

In Fig. 40 we show the median instead of the mean temperature. The changes are now much smaller, except near log overdensity = 1.7 where we see the peak temperatures and no sign of convergence as we decrease the cell size.

In Fig. 41 we show how the power of the flux depends

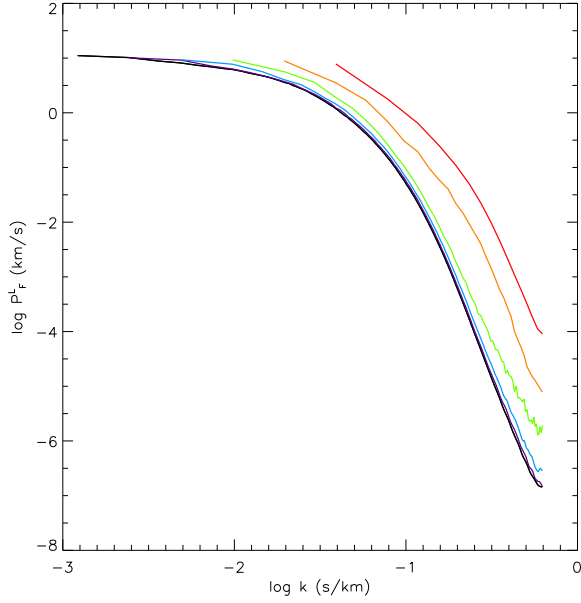


Figure 35. The 1D power spectra of the flux where the signal is divided by the mean flux in each sight line, and not the mean of the box. Compare to Fig. 16 that is identical except that there we divided the flux in each spectrum by the mean flux in the simulation box.

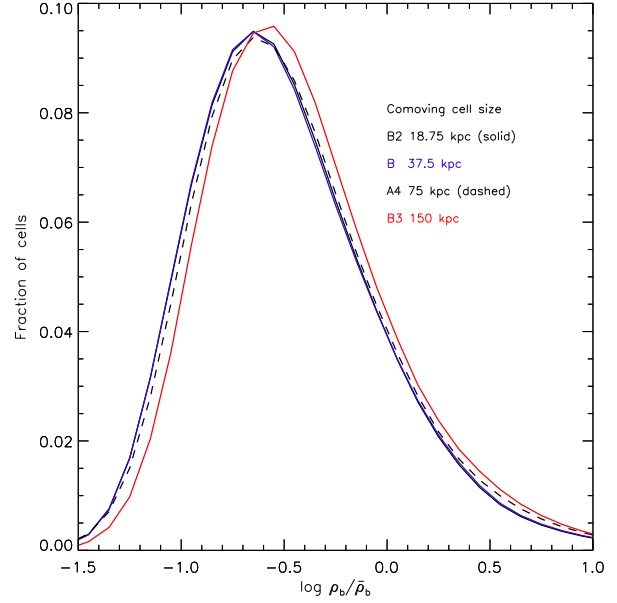


Figure 37. The pdf of the log baryon overdensity per cell for the B series simulations which differ in only their cell size. We show the fraction of cells sampled in intervals of $\log \rho_b / \bar{\rho}_b = 0.1$.

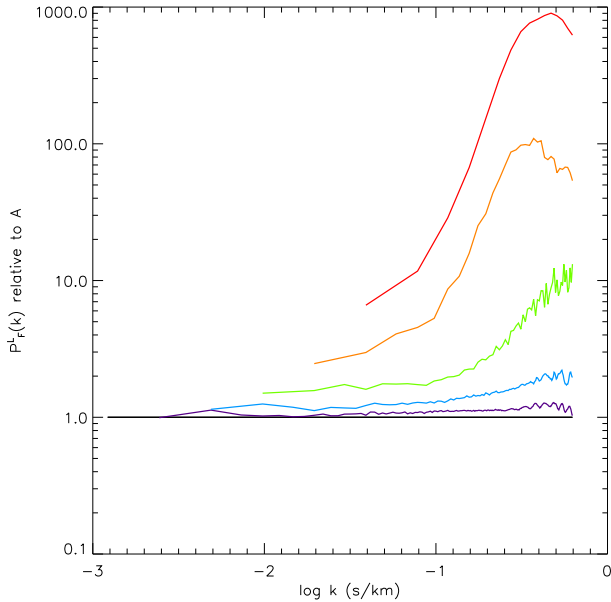


Figure 36. The 1D power spectra of the flux where we divided the flux in each spectrum by the mean flux in that spectrum. As Fig. 35 but now we divide the power by that in the A box. Compare to Fig. 17 where we divided each spectrum by the mean flux in the whole box.

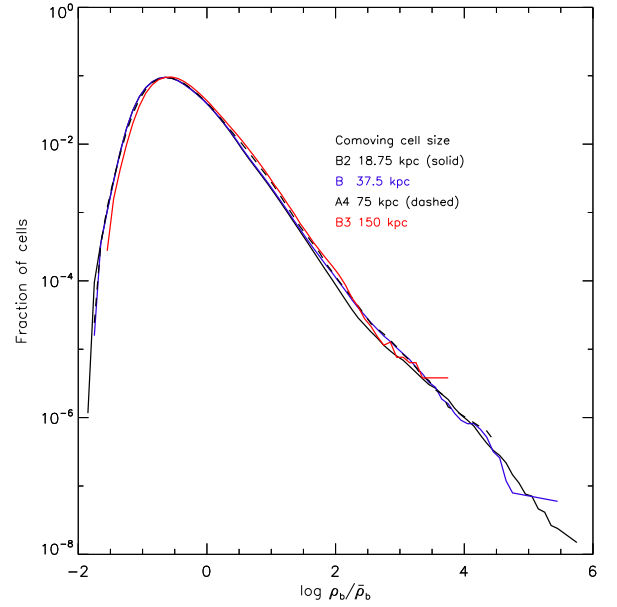


Figure 38. As Fig. 37 but with a log scale vertically. We sample in bins of size 0.1 in the log baryon overdensity. Simulations with smaller cells contain larger densities and extend farther to the right.

on the cell size. With smaller cells there is less power on the largest scales and more on small scales. The boxes with smaller cells begin with more power in total because their power spectra extend to smaller scales. Their structure becomes non-linear on small scales earlier and this encourages the growth of power on small scales at the expense of large ones.

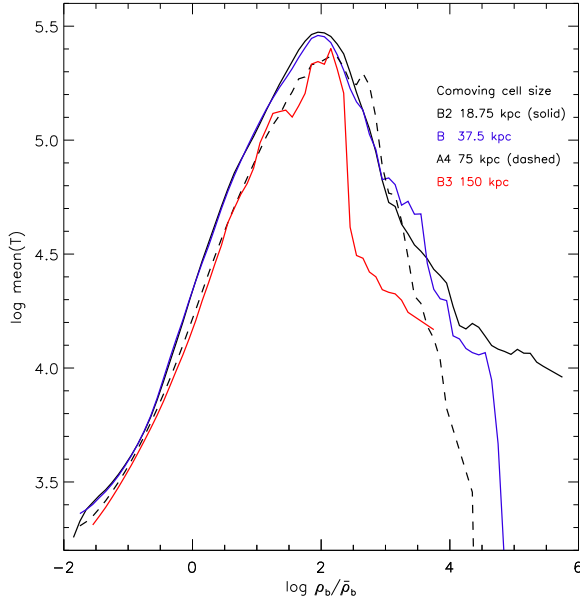


Figure 39. The mean temperature of cells as a function of the log baryon overdensity, sampled in bins of log overdensity 0.1.

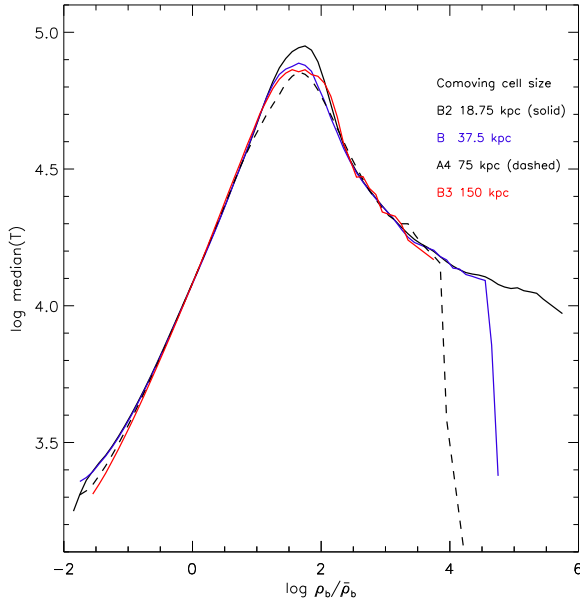


Figure 40. As Fig. 39 but showing the temperature that is exceeded in 50% of cells, the median, sampled in bins of log overdensity = 0.1.

In Fig. 42 we show the ratio of the power of the flux to the power from the B2 simulation that has the smallest cells. In general, the boxes with smaller cells have smaller flux power on the largest scales (small k) and more power on the smallest scales. We see that the maximum k value at which the power is larger than in B2 shifts systematically to higher values with the smaller cells: from -1.32 s/km (B3, 150 kpc cells) to -1.0 s/km (A4, 75 kpc cells) to -0.5 s/km (B, 37.5 kpc cells). We see that factor by which the power is

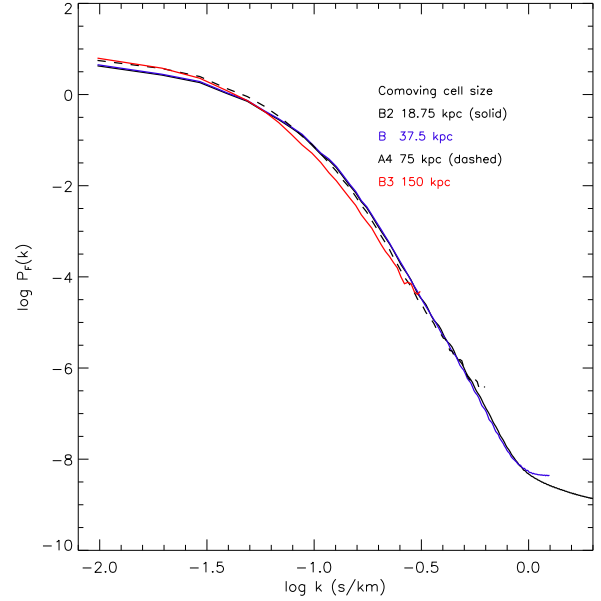


Figure 41. The 1D power spectra of the flux of the B series simulations which differ in only their cell size. We divided the flux in each spectrum by the mean flux in that simulation box. We terminate the power spectra at the Nyquist frequency for that cell size: B3 (150 kpc cells, $\log k = -0.5$, red line), A4 (75 kpc, $\log k = -0.2$, dashed black line), B (37.7 kpc, $\log k = +0.1$ s/km, blue line), B2 (18.75 kpc, $\log k = 0.4$ s/km, black line).

larger than in B2 on large scales (small k) is approximately constant over a range of k values, at approximately 1.35 for A4 and 1.07 for B. This suggests rapid convergence as the cell size decreases below 18.75 kpc. However, the convergence on smaller scales is much less rapid. The ratio of the power to that in B2 is a minimum on scales near a factor of two larger than the Nyquist frequency. These minimum values for the power ratios are large and approach 1.0 slowly as we decrease the cell size: from 0.52 (B3) to 0.75 (A4) to 0.83 (B). This behaviour suggests that cells smaller than 10 kpc will be needed to get the power at $\log k \simeq 0$ s/km to within a factor of 0.9 of the value in a simulation with much smaller cells.

One other feature of the power spectra of the flux is more troubling. We see that the power increases steeply on the smallest scales, just above the Nyquist frequency. We saw similar behaviour in Fig. 16 for the A series. Early in this investigation we saw much larger versions of these upturns in power which were caused by errors in the generation of spectra that lead to discontinuities in the flux. We continued searching for errors and found no more. However, the behaviour is clearly not physical, because simulations with smaller cells do show that the power ratios continue to decline smoothly on decreasing scales. We should not use the power from these simulations on scales within $\log k = 0.2$ s/km of the Nyquist frequency.

McDonald (2003, Fig. 6) shows how the power of the flux varied for three hydro-PM simulations (no shocks) in 6.25 Mpc boxes with cell sizes of 24.4, 48.8 and 97.6 kpc. While we both see that the largest cell size gives results very different from intermediate sizes (50 – 75 kpc), we do not

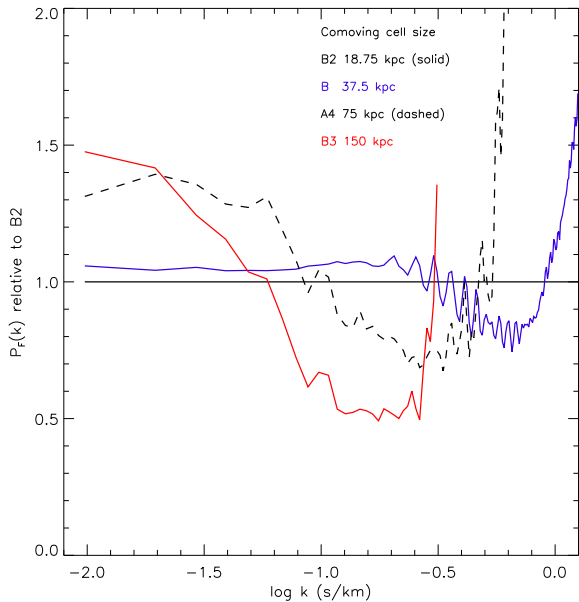


Figure 42. As Fig. 41 but showing the ratio of the power of the flux to the power from the B2 simulation. On the far left the simulations are from the top B3 (150 kpc cells, red line), A4 (75 kpc, dashed black line), B (37.7 kpc, blue line), B2 (18.75 kpc, black line at 1.0).

see much else in common between our results. This confirms the point made by McDonald (2003), that the results of resolution studies depend on the nature of the small scale force calculations and physics.

In Fig. 43 we see that the b -value distributions moves to significantly smaller velocities with smaller cells, except for B2 which has slightly larger velocities than B, reversing the trend. In Table 6 we list the b_σ values for the Hui-Rutledge fitting formula. The Δ column shows that the b_σ value drops 4.2 km s^{-1} from 150 to 75 kpc cells, and then 2.0 km s^{-1} going to 37.5 kpc, but it increases by 0.2 km s^{-1} going to 18.75 kpc cells. Since the internal error in the measurement is about 0.8 km s^{-1} , 35 kpc cells seem to give a fair estimate of the b_σ that would apply to a simulation with much smaller cells. The fitting function gives an excellent representation of the b -value distributions. In detail we see systematic differences between these distributions and the function, e.g. the function is too high around the most common b -values (especially for the larger cell sizes) and has too many lines with $b > 40$ (for B2, B) or $> 50 \text{ km s}^{-1}$ (for B3). As for the A-series, we use only lines with $b < 40 \text{ km s}^{-1}$ when we estimate the b_σ values.

In Fig. 44 we see that the simulations with smaller cells have factors of several more Ly α lines with the lowest column densities $\log N_{\text{HI}} < 13 \text{ cm}^{-2}$. However, the small cells also give about 20% fewer lines with $13 < \log N_{\text{HI}} < 17 \text{ cm}^{-2}$ where the precise range depends on the cell size. Hence simulations with smaller cells are slightly farther from data than was simulation A (75 kpc cells) that has too few lines of high $\log N_{\text{HI}}$ (Fig. 15).

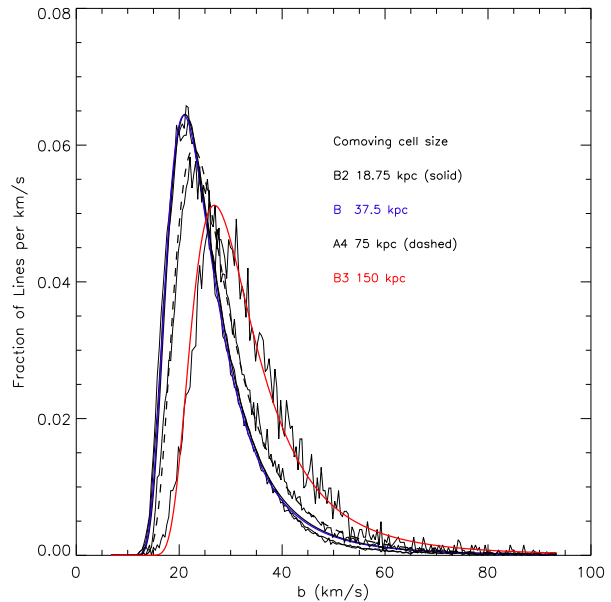


Figure 43. The distribution of the b -values for Ly α lines with $12.5 < \log N_{\text{HI}} < 14.5 \text{ (cm}^{-2}\text{)}$ and line central optical depth $\tau > 0.05$ in B series simulations. The jagged thin lines are the distributions of the values and the smooth curves are the Hui-Rutledge fits to each pdf. From the right, at a fraction of 0.004, the simulations are B3 (150 kpc cells, red line), A4 (75 kpc, dashed black line), B2 (18.75 kpc, black) and B (37.7 kpc, blue line) which is out of order and largely hidden under B2.

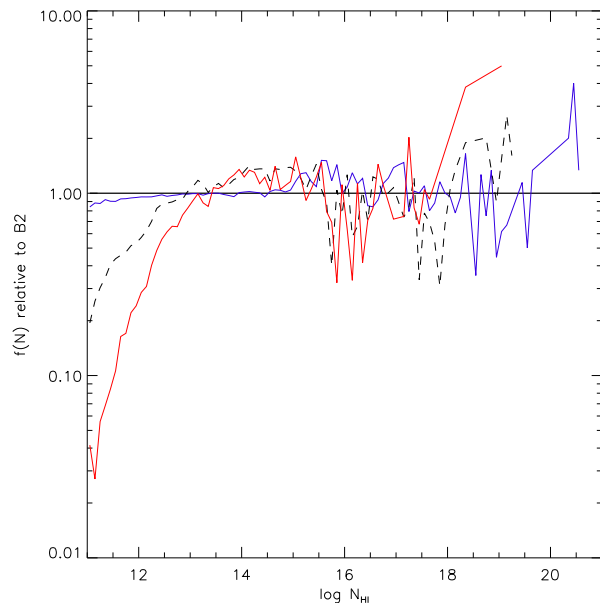


Figure 44. How the column density distribution depends on the cell size of a simulation. We show the $f(N)$, measured using all lines with line central optical depth $\tau > 10^{-5}$. Here only we evaluate $f(N)$ per unit z rather than X , and we divided by the $f(N)$ from the B2 simulation. We give values for evaluated in bins of width 0.1. On the far left the simulations are from the bottom B3 (150 kpc cells, red line), A4 (75 kpc, dashed black line), B (37.7 kpc, blue line), B2 (18.75 kpc, black line at 1.0).

Table 11. The Convergence of Statistics of the A series. The ratios are of quantities from smaller boxes A4, A3 or A2 to the value in the largest box A. When a range is indicated, we list the largest value in that range.

Quantity	A4/A	A3/A	A2/A
Flux mean	1.0031	1.0023	1.0008
Absorption = 1- flux mean	0.9790	0.9844	0.9946
Flux pdf (F=0.995-1.0)	0.62	0.81	0.93
Flux pdf (F=0.8)	1.24	1.13	1.05
Typical line width b_σ (km s ⁻¹)	0.903	0.929	0.959
$f(N)$ log N _{H I} = 12.5 - 14.5	0.83	0.85	1.10
$f(N)$ log N _{H I} = 15	0.73	0.81	0.84
Flux P(k=0.01)	0.966	1.023	0.959
Flux P(k=0.1)	1.465	1.194	1.074
Frequency of CDM density	0.93	1.03	0.98
Mode CDM density	0.2	0.2	0.50

Table 12. Comparison of Statistics from Simulation A to those from Data. The column headed “A” lists the value of the quantity in box A. The column A2-A lists the value of the parameter in box A2 minus the value in box A. The errors on the data values are guessed, not precise, values.

Quantity	A	A2-A	Data	$\sigma(\text{data})$
Flux mean	0.8714	-0.0007	0.869	0.01
b_σ (km s ⁻¹)	26.7	1.1	23.6	1
$\log f(\log N_{\text{HI}}=14.3)$	-13.49	-0.03	-13.39	0.2
Flux P(k=0.01)	5.8	0.23	7	1
Flux P(k=0.1)	0.049	-0.004	0.13	0.05

10 CONVERGENCE AND COMPARISON WITH DATA

In Table 11 we summarise the convergence trends that we see in the simulation boxes, and in Table 12 we compare the difference between the values seen in A and A2 with the likely error from measurements of data.

We see very small changes in the mean flux with increasing box size, in part because the amount of absorption is small compared to the mean flux. The changes are better seen in the amount of absorption itself. The rate of convergence suggest that the mean flux in A is within 0.0007 of the value expected in a much larger simulation. This is about a factor of 14 better known than the measurement error of approximately 0.01, from continuum level errors and difficulties removing absorption from metal lines and strong Ly α lines down to some fixed N_{H I} value (Tytler et al. 2004; Kirkman et al. 2007; Kim et al. 2007). The mean flux in simulation A is essentially identical to that from Eqn. 10 of J05, scaled to $z = 2$, and we expect this to remain true in a much larger box.

For the flux pdf, Figure 11 indicates that simulation A will be within about 5% of the frequencies for a much larger simulation. For b_σ the error from the simulation box size is comparable to that for data. The Δ values in Table 6 do not show much evidence for convergence, since the change in b_σ from A2 to A is larger than the change from A3 to A2, and from A4 to A3. This slow convergence can be traced back to the effects of the long modes of the CDM density fluctuations that change the size of the absorbing regions, the velocities and the temperatures.

We also see that the b_σ for A is significantly larger than for data (Kim et al. 2001; Jena et al. 2005) and the difference will be still larger in a larger box. We can estimate the change in b_σ if we had run simulation A with a resolution of 20 kpc instead of 75 kpc, using the scaling relations given in J05; the value of b_σ would change from 26.7 km s⁻¹ to 25.1 km s⁻¹. To better match data, we need a simulation with less heat input (smaller X_{228}) or larger σ_8 (Figs. 21 and 38 of J05), which is a surprise since the value we are using, $\sigma_8 = 0.9$, is large compared to the WMAP 3-year suggestion. We (Tytler et al. 2004; Jena et al. 2005) and others (Viel et al. 2006; Seljak et al. 2005; Viel et al. 2007) have previously noted that the Ly α forest data prefer much larger σ_8 values than does the CMB anisotropy. Slosar et al. (2007) use Ly α forest, Supernovae and galaxy clustering data with WMAP 3-year data to estimate $n = 0.965 \pm 0.012$ and $\sigma_8 = 0.85 \pm 0.02$, compared to $\sigma_8 = 0.80 \pm 0.03$ without the Ly α forest.

The changes that we will need to make to the simulations match the column density distribution of data will also change the b -value distribution and the b_σ value. The minimum b -value in the Ly α forest increases as N_{H I} increases (Kirkman & Tytler 1997) until we reach log N_{H I} = 15 cm⁻² after which the values start declining in our HIRES spectra and in simulations (Misawa et al. 2004, Figs. 3, 5). Since simulations need fewer lines with log N_{H I} < 14 cm⁻² and, in compensation to conserve the total absorption, more at 14 < log N_{H I} < 15 cm⁻² (Fig. 15) the mean b values will increase, exacerbating the differences with data.

The lack of high column lines is the second conspicuous difference between our simulations and data. As noted previously, this is due to insufficient spatial resolution and lack of self-shielding in collapsed dense halos. In Fig. 15 we saw that our simulations have too many lines with log N_{H I} < 14 cm⁻², a slight lack of lines, with log N_{H I} = 14–15 cm⁻², and a large lack with log N_{H I} > 17 cm⁻². This lack of high column lines will reduce the power to below that in real spectra that include such lines. We also noted that our sight lines that are parallel to the box sides are too short to contain the full damping wings of DLAs. Fig. 14 shows convergence as the box size increases and suggests that the $f(N)$ values from simulation A for log N_{H I} = 12.5–14.5 cm⁻² are within about 10% of the values we would obtain from a much larger box.

In Figs. 45 and 46 we compare the power of the flux of the Ly α forest in data to that in our simulations. The power from the simulations is less than in the data at all k values. The power in the simulations is too low by about 20% at $-1.6 < \log k < -1.1$ km s⁻¹ rising to about 50% on large scales at log $k < -2$.

We are most concerned about the missing power on large scales. There we have SDSS measurements that we trust more than those from J05 on small scales, and there should be no problems from residual metal lines in the real spectra at large scales. The values that we give for the errors on the power on the data in Table 12 are guesses based on the spread between different measurement values. We note that the differences between the simulation and data seem less at large k since only a small change in k would be needed to align the two. However, the errors on k are very small, and hence we are interested in the vertical change in the power and not a horizontal shift in k .

We had expected the power of the simulation to be

smaller than in data on small scales (large k) because the b -values in the simulations are larger than in data. The sense of the differences are consistent: larger b values correspond to less power at $\log k > -1.5$ s/km Viel et al. (2003). We also knew that we lacked large scale power when we began this investigation and we had hoped to understand this difference, but we have not.

A major conclusion of this paper is that a much larger box will not bring the power from the simulations up to that in the data since we saw in Fig. 17 that the effects of doubling the box size are ten times smaller than the amount of missing power.

We have also shown that improving the resolution of the simulations by reducing the cell size makes the problem much worse at large scales. In Fig. 42 we saw that when we decrease the cell size, from 75 kpc to 18.75 kpc we decrease the power in the simulation at $\log k < -1$ s/km, by 30 – 40% at the largest scales. Using these small cells, the power in the simulation is then about a factor of two (1.5×1.35) below that in data. Simultaneously, the power increases for the largest few k values, which brings the simulation closer to the data. The power from the B2 simulation is the lowest of all in Figs. 45 and 46 and yet it has the same input parameters and box size as A4 and 4 times smaller cells than the A series. In J05 we noted that B2 has a lower b_σ value (corresponding to higher small scale power) but higher mean flux (lower power) than the A-series. Hence to better match data we should re-run B2 using a lower γ_{912} to increase the Ly α absorption and this will increase the power a bit.

We know that our simulations have too many low column density lines and too few with high column densities. When we used cells 4 times smaller, these differences got worse, as did the difference in the power. We also noted that a four times reduction in cell size does not correct the large lack of lines with $\log N_{\text{HI}} > 17 \text{ cm}^{-2}$, lines that we hope are excluded from the data. Kohler & Gnedin (2007) showed that they obtain the correct number of such LLS using 2 kpc cells. We are curious whether 2 kpc cells might also match the entire column density distribution and perhaps the power.

10.1 What Cell Size do we Need?

We know from our analysis of the KP series of simulations in §7 that we can mimic much of the effects on the Ly α forest of doubling the size of a box by instead increasing the X_{228} parameter that increases the heat input per He II ionization. We must simultaneously decrease the rate of H I ionizations by reducing the γ_{912} to bring the amount of H I back to the level that gives the observed mean flux value. Small simulation boxes are too cold compared to large ones.

In Figs. 37 and 38 we saw that there was very little change in the pdf of the baryon density per cell, for typical densities, going from 37.5 to 18.75 kpc cells, implying that 37.5 kpc is acceptable for our work.

In Fig. 40 we see no convergence by even 18.75 kpc for the median temperature at log baryon overdensity near 1.7. Smaller cells are leading to higher median temperatures. Fig. 39 however shows that mean temperatures are converged by 18.75 kpc, again suggesting that 37.5 kpc is small enough for the current work.

In Fig. 42 we saw that changing the cell size from

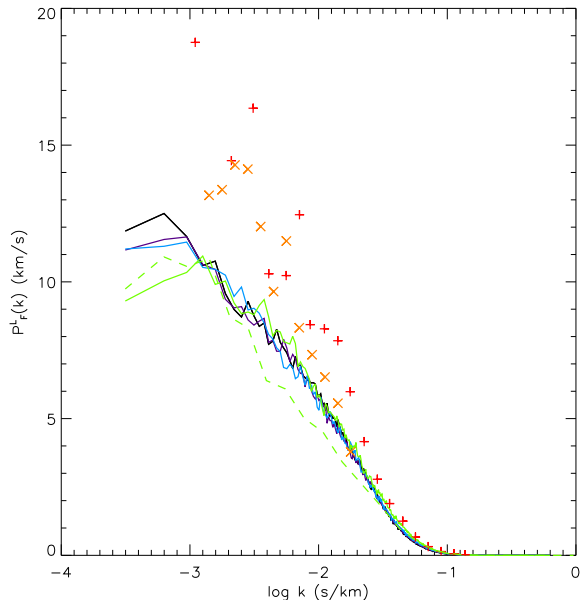


Figure 45. Comparison of the power of the flux in the Ly α forest with that for our simulations. Lines show the power of spectra from simulations A (black), A2 (violet), A3 (blue) and A4 (green), our usual colour scheme. The dashed green line is for simulation B2 from J05. We use flux spectra that travelled in random directions for a distance of $\delta z = 0.2$ (Appendix C), but without evolution of the IGM (Appendix B). We divided all spectra by the mean flux in that spectrum, to match what was done with the data. We show the power from McDonald et al. (2006) linearly extrapolated to $z = 2$ (orange x) and the PJ05 power (J05 §6.4) from 6 HIRES and UVES spectra (red +) with metal lines masked.

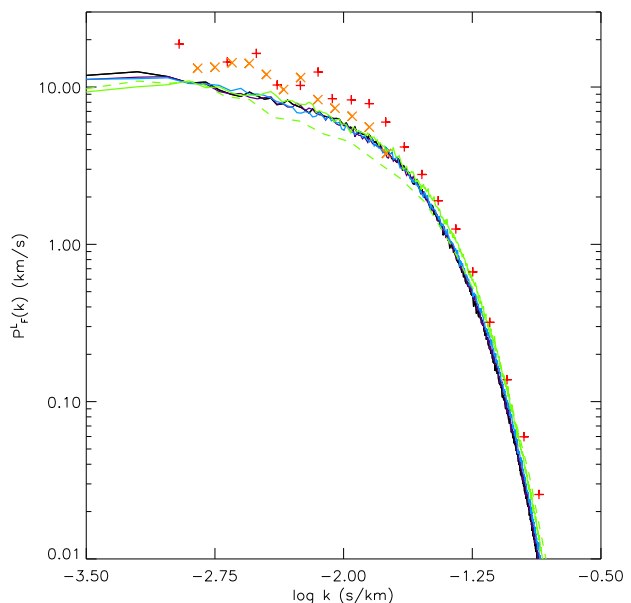


Figure 46. As Fig. 45 but on a log scale.

75 kpc to 18.75 kpc has a complex effect on the power spectrum. The power drops by 30 – 40% on large scales ($\log k < -0.7$ s/km) but then increases by up to 30% before falling again on the smallest-scales near the Nyquist frequency.

In Fig. 43 we saw that the b -value distribution changes noticeably from 150 to 75 to 37.5 kpc cells, but the change going to 18.75 kpc is barely detectable. This implies that the sensitivity of the small scale power to decreasing the cell size below 37.5 kpc has little effect on the Ly α lines.

In Fig. 44 we saw that using 37.5 kpc rather than 18.75 kpc cells made the column density distribution too low by about 5% at $\log N_{\text{HI}} = 12 \text{ cm}^{-2}$ and too large by 20% at $15 < \log N_{\text{HI}} < 17 \text{ cm}^{-2}$.

In summary, a cell size of 37.5 kpc is probably adequate at this time, but smaller cells (or correction factors) will be needed for the highest accuracy work. We will definably need to apply corrections if we use cells of 75 kpc or larger.

10.2 How Large a Box do we Need?

We summarise by ranking the statistical parameters in the order of increasing difference of the A2/A values from unity. The mean flux (1.0008), amount of absorption (0.995), and the frequency of the CDM density (0.98) are the most converged quantities. Then follow the b_σ (0.96), the flux pdf (1.05, 0.93) and the power of the flux (0.96, 1.07). The $f(N)$ (1.10, 0.84) is less converged and the mode CDM density (0.50) shows no sign of convergence in our boxes.

Some of the CDM statistics converge while others do not. In Fig. 2 we see convergence in the frequencies of the CDM densities. We also see convergence with the power of the CDM density in Fig. 5, however the mode of the CDM density distribution in Fig. 4 shows no sign of converging as the box size increases. We discussed how this was caused by the rare very high density regions in the larger boxes. These high density regions are not in the low density IGM and yet they dominate many of the CDM statistics, including the power and the pdf.

To first order, the values in Table 11 show that doubling the size of a box typically halves the difference of a parameter value from its value in the largest box. If this trend were to continue unchanged, we know from the sum of the geometric series $1/2 + 1/4 + 1/8\dots$ that the value in a very large box would be approximately the value in A plus the difference from A2 to A. In practice we can expect the series to converge more quickly as the box size increases past several hundred Mpc to include the peak in the matter power (Bagla & Ray 2005). Hence the values of the parameters in a very large box would be similar to the value in A plus the value in the column A2-A in Table 12.

If the b -values converge as do the other statistics, which we have not established, then we might guess that a much larger box, many hundreds of Mpc in size, with 20 kpc cells would give $b_\sigma = 25.1 + 1.1 = 26.2 \text{ km s}^{-1}$ that is 2.6 km s^{-1} larger than the data.

This comparison with the measurement errors for data suggests that the box size is a relevant but probably not the dominant error for our largest box. The only exception is the line widths where the difference between the values from our two largest boxes is similar to the measurement error. We would like factor of several larger boxes to reduce

this uncertainty. Since the b -values are closely related to the small scale power, we would expect that larger boxes will also bring useful improvements in the accuracy of the small-scale power.

We can most easily detect the increase in the size of a simulation box in data on the smallest scales, the Ly α line widths. This is primarily because it is easier to make high accuracy measurement of small scale features of the Ly α forest than of the large scale trends, such as the power of the flux.

11 PHYSICAL EXPLANATIONS

We have deliberately treated the simulations like observational data. We concentrated on reporting how statistics that describe the IGM and the Ly α forest change with box size. We have resisted the temptation to follow additional side line investigations that might reveal the physical causes of these effects. We now give a short discussion of the possible physical explanations for the changes that we see with box size.

The larger boxes differ from smaller ones in only two ways; they contain more cells and they contain longer mode perturbations that do not fit in the smaller boxes. The extra modes add more power in total to the simulations, leading to larger velocities and more kinetic energy. We will see flows that are coherent on larger distances, and larger velocity differences on a given distance scale. Changes in the (negative) gravitational potential energy are more complex. Potential wells become deeper where long modes are positive density fluctuations, and shallower elsewhere, giving a cancellation to first order. We saw in Figure 2 that non-linear effects lead to rather complex changes in the CDM density per cell. We saw a decrease in the number of cells near and above the most common density and an increase in the number of lower density cells.

We hope to explain, using the longer modes alone, all the changes that we see with box size. We see changes in both the elemental density, velocity and temperature fields and in the various Ly α forest statistics that are composites of these fields.

We saw in Fig. 5 that by $z = 2$ the longer modes have evolved to add power on all scales, but especially the largest ones. This is a Richardson-Kolmogorov cascade (Kritsuk et al. 2007) of energy from large to small scales, which is a non-linear effect. The study of Bagla & Ray (2005) shows the growth in the number of halos as a result of this cascade, where they use a fixed box size and truncate the initial power to sub-box scales. We do not know the extent to which these results are sensitive to the finite box size, the box shape and the periodic boundary conditions.

11.1 Why the gas causing the Ly α forest is hotter in larger boxes

The gas in the IGM that causes the Ly α forest is hotter in the larger simulation boxes because the enhanced heating by shocks has a larger effect than the increased adiabatic cooling because the gas is less dense. We now discuss why we believe this.

We have discussed how the extra longer modes evolve to

give more power on all scales, and we expect larger velocities. The most obvious explanation is that the increased density and velocity perturbations lead to faster collisions of gas, and increased virialisation temperatures. This thermalisation effect also applies to the warm-hot IGM at $z \simeq 0$ that is not seen in H I absorption, but it is less clear how important it is for the IGM that produces the Ly α forest at high z . Most cells in the IGM have not been in any collisions by $z = 2$, and hence we require that the heat from collisions spreads far beyond the cells that contain the shocks (Cen & Ostriker 1999; Davé & Tripp 2001).

A second class of explanations is that the larger boxes are hotter because the gas that makes the Ly α forest has cooled less than in the smaller boxes. The IGM is heated when H I, He I and He II are ionized. The temperature drops in time due to Hubble expansion. Lower density regions expand faster and cool more, leading to the well known increases in temperature with density for the gas causing the Ly α forest (Hui & Gnedin 1997), as illustrated for two of our simulations in Tytler et al. (2004, Fig. 19) and Fig. 34 of J05. The longer modes in larger boxes may give rise to higher densities that reduce the adiabatic cooling from Hubble expansion. The gas that makes Ly α forest lines is hotter in larger boxes because it expands less and cools less.

However, this can not be the entire explanation. When we add the longer modes we make some densities higher and others lower. We expect the two to give opposing effects that will tend to cancel to first order. This mechanism might explain the net heating of the IGM because the long modes make a larger increase in the number of hotter cells than in the number of cooler cells. The asymmetry favouring heating comes from the distribution of the number of cells as a function of density. There are more cells at lower densities, and hence when the long modes adjust all densities, there is a net flow of cells to higher density. We can see the pdf of cells as a function of density in Jena et al. (2005, Fig. 34) where the most common baryon density is near 0.2 of the mean density, below the typical density that leads to lines with $\log N_{\text{HI}} = 12.5 \text{ cm}^{-2}$. This asymmetry is a version of the Malmquist bias, in which we see a net increase in the number of objects detected in a flux limited sample (Gonzalez & Faber 1997). The effect depends on the steepness of the pdf of the flux, or in our case the pdf of the density of cells.

We saw in Fig. 29 that larger boxes had a smaller fraction of their cells in the density range responsible for the Ly α forest. The temperature depends on the relative number of cells with different densities. In Fig. 30 we saw that there is a larger decrease in the number of cells with $\log \delta_b \simeq 0$ compared to cells with $\log \delta_b \simeq 1$, except for the smallest box. Since the lower densities correspond to lower temperatures, we then expect the larger boxes to have fewer cells with cooler densities, although the changes are small.

In Figure 14 we saw that in larger boxes the column density distribution has relatively more lines near the higher end of the $12.5 - 14.5 \text{ cm}^{-2}$ range that we use when we measure b_σ . Such lines tend to have larger b -values. We do not know if the b -value pdf changes at a given N_{HI} , or if we can explain the larger b_σ entirely in terms of the change in $f(N)$.

In summary we do not find any convincing evidence for the second explanation, that the Ly α forest lines are wider

in larger boxes because they come from gas that cooled less. Rather we prefer the first explanation, that the larger boxes are hotter because the velocities are larger giving more and stronger shocks.

11.2 Why the Ly α forest lines are wider in larger boxes

Ly α line widths are set by three components (Bryan et al. 1999), thermal from the gas temperature, peculiar velocities from hydrodynamical motions and Hubble from the cosmological expansion (Sargent et al. 1980). We have shown in Figs. 20 and 24 that the gas temperature and peculiar velocities increase with box size for fixed photoionization and cosmological parameters. Hubble broadening depends on the size of the line forming regions which in turn depends on the balance between the previous two gas attributes. High temperature leads to thermal expansion and larger lines, while increased peculiar velocities are indicative of high compressions that tend to decrease the size. In Bryan et al. (1999) it was determined that in the column density range relevant to the b -parameter distribution ($10^{12.5} - 10^{14.5} \text{ cm}^{-2}$) thermal broadening increasingly dominates over Hubble broadening at larger column densities. Therefore we conclude the Ly α forest lines are wider in the larger boxes because thermal and peculiar velocity effects.

11.3 How might we make simulations with the appropriate temperatures

We discuss several potential ways of making the IGM in our simulations cooler and closer to the temperature required by Ly α forest data.

First, we should mention that there remains a slight possibility that there is no problem with the IGM temperature, and rather a mis-match in the comparison of the simulation and data because the b -value distributions are not determined using the same codes.

We have seen that increasing the resolution of our simulations does lead to a cooler IGM with smaller b -values. However, we can not run the ideal simulation. A simulation with 18.75 kpc cells (like B2) in a 76.8 Mpc box (like A) would have 8192^3 grid cells, a factor of 4^3 too large for the supercomputers we use. An adaptive mesh refinement (AMR) simulation with increased resolution at the densities of interest is also not practical. Areas of interest in our case is the filamentary structure which corresponds to overdensities above 1. A simulation of the 76.8 Mpc box would require three levels of refinement (increase of resolution by a factor of 2 for each level) to have an effective resolution equal to that of the B2 case at overdense regions. However, the volume fraction of regions with densities above the cosmic mean is quite significant and that would have required a prohibitive number of refinement subgrids.

The temperature of the IGM at ionization is set in large part by the mean energy of the photons that cause the ionization. Softer spectra have steeply declining numbers of photons with increasing energy above the ionization threshold. We could make the temperature lower by using an ionizing spectrum that was softer than that specified by Haardt and Madau, at either 1 Rydberg for H I or 4 Ry for He II or for both.

Early results from simulations that include the effects of radiation transfer suggest that this makes the IGM hotter and exacerbates the difference with data. Paschos et al. (2007) have carried out an approximate treatment of the helium ionization due to discrete QSO sources and have found out that the temperature of the IGM at the cosmic mean density can be on average 68% above in an optically thin simulation. This increases the widths of Ly α lines by only about 1.3 km s^{-1} at $z = 2.5$, because other factors (Hubble flow, turbulence) dominate the line widths. Bolton et al. (2004) also found an increase in the IGM temperature in their radiative transfer calculation. Hence adding radiative transfer seems to make Ly α lines still wider, exacerbating the difference from data.

We could also decrease the temperature by decreasing the He/H abundance ratio. For our Haardt and Madau UVB spectrum, more heat is input per baryon when the baryons are in ^4He rather than in ^1H . Since He is ionized later than H, if we decrease the number of baryons in He we decrease the temperature at $z = 2$. However, constraints on the primordial He abundance from standard big bang nucleosynthesis, from CMB anisotropy constraints on the baryon density and from observations of the He abundance in extragalactic H II regions all make this suggestion a long shot.

The IGM will be cooler at $z = 2$ if we ionize it earlier since the temperature of the IGM is set in part by the amount of expansion following the ionization. We show now that the effect is too small to be relevant to us. Again, we could make the ionization of either H I or He II or both occur earlier. We do this by increasing the intensity of the UVB at early times. Integrated over time from the earliest z we then need more photons to reach a given ionization at $z = 2$ because recombinations are faster when the IGM is denser. However, we find that although cosmic expansion tends to cool down the IGM, it is the more rapid increase of the UV background intensity with decreasing redshift, as computed by Haardt & Madau, that dominates the thermal state of the gas at late redshifts. We demonstrate this in Fig. 47 where we show how the mean temperature of the IGM changes with the epoch of reionization. These results are from three simulations in $100 h^{-1} \text{ Mpc}$ boxes each with 128^3 cells. We use the Haardt & Madau ionizing spectrum described in §2. We use a very steep function to increase the flux from zero to the normal intensity at some high z . When we initiate the ionizing flux at redshifts 7, 8 or 9, the mean temperature is barely changed for all $z < 5$. These results differ from Miralda-Escudé & Rees (1994, Fig. 2) who found a steep decrease in temperature with decreasing z because they used an ionizing spectrum that was continuously decreasing in intensity, and not now favored by data.

Lastly, we can change the Ly α line widths by changing the amplitude (σ_8) and shape (n_s) of the primordial power spectrum. Fig 21 of J05 shows that a larger σ_8 to match the large-scale power of data will also make the b -values smaller, as needed to match data.

We know from J05 that simulation A4 has approximately the correct b -values. The temperature of the IGM at $z = 2$, and at the mean baryon density, may be close to 12,000 K if $\sigma_8 = 0.9$ and we neglect radiative transfer. We expect a higher temperature is needed to match data if $\sigma_8 > 0.9$.

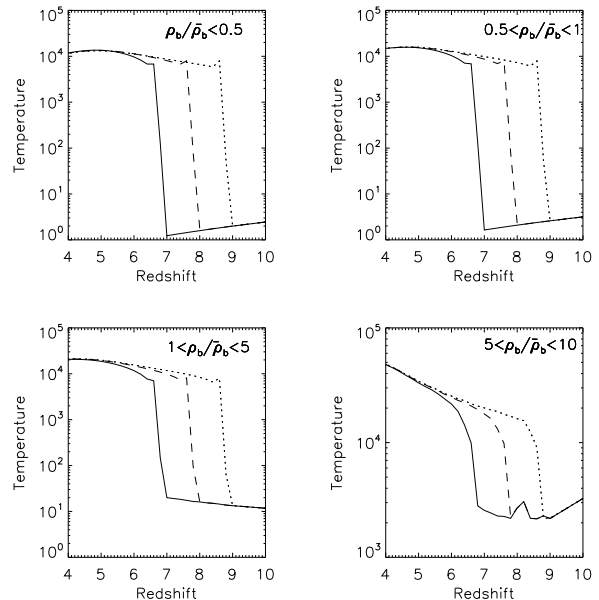


Figure 47. The mean temperature (in K) of the IGM as a function of the epoch of reionization. The four panels from the upper left show the mean temperatures for increasing ranges of density. We use a different scale at the highest densities in the lower right because they are at higher temperatures.

11.4 Why do the simulations lack large scale power?

We have seen that relative to Ly α forest data our simulations lack power on all scales, especially the largest ones and their lines are too wide. We also noted that the simulations have a different $f(N)$ distribution from the data, especially a lack of lines with $\log N_{\text{HI}} > 17 \text{ cm}^{-2}$.

We discussed in §4.2.2 whether simulations with more absorption from lines with $\log N_{\text{HI}} > 14 \text{ cm}^{-2}$ and especially > 17 , would have more power on large scales, and perhaps enough to match data. We do not know if matching the $f(N)$ distribution will exactly match the power spectrum. If this were to fail, there would remain at least three other parameters that could change the power: the amplitude (σ_8) and slope (n_s) of the initial power, and the temperature of the gas (X_{228}). We would have to simultaneously adjust the γ_{912} to maintain the observed amount of H I absorption, which does match data. Our simulations use relatively high values for both $\sigma_8 = 0.9$ and $n_s = 1.0$, and a best guess for the heating by the UVB.

The power in the simulations could be below the data because of errors in the data. The power of the data presented in J05 (PJ05) include only Ly α lines (no metals) with $\log N_{\text{HI}} < 17.2 \text{ cm}^{-2}$, hence they should be directly comparable to the simulations, but they may still contain some metal lines. In J05 we noted that the PJ05 power spectrum values could be too large, because they are 30% larger than our estimates of the power from Kim et al. (2004a) after we removed the power from metal lines. However, the SDSS measurement of power should be as reliable as any current measurement, and the SDSS power is very similar to that from J05.

The most obvious way to increase the large-scale power

in the simulations is to increase σ_8 above the large value of 0.9 that we used. We saw in Fig 21 of J05 that larger σ_8 values also give smaller b -values, as required to better match data. We expect that larger σ_8 also gives larger small scale power, because the lines are narrower. However, McDonald et al. (2002, Fig. 10a) found the opposite, perhaps because his simulations use simpler representations of small scale physics.

We should also investigate changing the power spectrum tilt or shape. McDonald et al. (2002, Fig. 10a) suggests that decreasing the slope from $n = 1.0$ to $n = 0.95$ will increase the large-scale flux power in simulations by about 6%, which is the desired direction of change, but much less than the factor of two increase needed to match data.

12 SUMMARY OF THE COMPARISON WITH DATA

Our simulations differ from data in at least three ways: their b -values are too large, they have too few many lines with $\log N_{\text{HI}} < 14 \text{ cm}^{-2}$ and too few with larger N_{HI} , and most conspicuously, the power spectra of their flux has too low an amplitude. We have found that increasing the box size does not help while decreasing the cell size, or adding radiative transfer both make the critical differences larger. A $\sigma_8 > 0.9$ is one way in which these simulations might match data.

While it is early to reach a conclusion, we do feel that there is a real difference between our simulations of the IGM and the data we are using. It is premature to conclude that we are adding too much heat, or that we need $\sigma_8 > 0.9$, because we do not yet understand why we do not match the power spectrum of the flux, and we need to be more careful when we excise high column density Ly α lines (and metals) from both data and simulations. However, it is looking increasingly difficult to make simulations that match the b -values, mean flux and flux power of the Ly α forest at $z = 2$ using popular values for the astrophysical and cosmological parameters.

ACKNOWLEDGMENTS

This work was supported by NSF grant AST 0507717. Simulations were produced using the facilities of the NCSA SDSC supercomputer centres with LRAC allocation MCA98N020. We thank Brian O’Shea for help with ENZO and we are extremely grateful to Pat McDonald for generously sharing his considerable experience and insights. We also acknowledge helpful discussion with Alexei Kritsuk, Avi Loeb, Mordecai Mac-Low, Joop Schaye and Paul Shapiro.

REFERENCES

Abel T., Anninos P., Zhang Y., Norman M. L., 1997, *New Astronomy*, 2, 181
 Anninos P., Zhang Y., Abel T., Norman M. L., 1997, *New Astronomy*, 2, 209
 Bagla J. S., Ray S., 2005, *MNRAS*, 358, 1076
 Barkana R., Loeb A., 2004, *ApJ*, 609, 474

Bodenheimer P., Laughlin G. P., Rózycka M., Yorke H. W., eds, 2007, *Numerical Methods in Astrophysics: An Introduction*
 Bolton J., Meiksin A., White M., 2004, *MNRAS*, 348, L43
 Bracewell R., 1986, *The Fourier Transform and its Applications*. McGraw-Hill
 Bryan G. L., Machacek M., Anninos P., Norman M. L., 1999, *ApJ*, 517, 13
 Bryan G. L., Norman M. L., 1997, in Clarke D. A., West M. J., eds, *Computational Astrophysics; 12th Kingston Meeting on Theoretical Astrophysics Vol. 123 of Astronomical Society of the Pacific Conference Series, Simulating X-Ray Clusters with Adaptive Mesh Refinement*. p. 363
 Bryan G. L., Norman M. L., Stone J. M., Cen R., Ostriker J. P., 1995, *Computer Physics Communications*, 89, 149
 Cen R., Ostriker J. P., 1999, *ApJ*, 514, 1
 Croft R. A. C., Gaztanaga E., 1997, *MNRAS*, 285, 793
 Croft R. A. C., Weinberg D. H., Katz N., Hernquist L., 1998, *ApJ*, 495, 44
 Davé R., Tripp T. M., 2001, *ApJ*, 553, 528
 D’Odorico V., Viel M., Saitta F., Cristiani S., Bianchi S., Boyle B., Lopez S., Maza J., Outram P., 2006, *MNRAS*, 372, 1333
 Eisenstein D. J., Hu W., 1999, *ApJ*, 511, 5
 Gardner J. P., Katz N., Hernquist L., Weinberg D. H., 2001, *ApJ*, 559, 131
 Gnedin N. Y., 1998, *MNRAS*, 299, 392
 Gnedin N. Y., Baker E. J., Bethell T. J., Drosback M. M., Harford A. G., Hicks A. K., Jensen A. G., Keeney B. A., Kelso C. M., Neyrinck M. C., Pollack S. E., van Vliet T. P., 2003, *ApJ*, 583, 525
 Gonzalez A. H., Faber S. M., 1997, *ApJ*, 485, 80
 Haardt F., Madau P., 2001, in *Clusters of galaxies and the high redshift universe observed in X-rays, Recent results of XMM-Newton and Chandra, XXXVIth Rencontres de Moriond, XXIst Moriond Astrophysics Meeting, March 10-17, 2001, Savoie France*. Edited by D.M. Neumann & J.T.T. Van Modelling the UV/X-ray cosmic background with CUBA
 Heitmann K., Lukic Z., Fasel P., Habib S., Warren M. S., White M., Ahrens J., Ankeny L., Armstrong R., O’Shea B., Ricker P. M., Springel V., Stadel J., Trac H., 2007, *ArXiv e-prints*, 706
 Heitmann K., Lukić Z., Habib S., Ricker P. M., 2006, *ApJ*, 642, L85
 Hockney R. W., Eastwood J. W., 1988, *Computer simulation using particles*. Bristol: Hilger, 1988
 Hui L., Burles S., Seljak U., Rutledge R. E., Magnier E., Tytler D., 2001, *ApJ*, 552, 15
 Hui L., Gnedin N. Y., 1997, *MNRAS*, 292, 27
 Hui L., Rutledge R. E., 1999, *ApJ*, 517, 541
 Janknecht E., Reimers D., Lopez S., Tytler D., 2006, *Å*, 458, 427
 Jena T., Norman M. L., Tytler D., Kirkman D., Suzuki N., Chapman A., Melis C., Paschos P., O’Shea B., So G., Lubin D., Lin W., Reimers D., Janknecht E., Fechner C., 2005, *MNRAS*, 361, 70
 Katz N., Weinberg D. H., Hernquist L., Miralda-Escude J., 1996, *ApJ*, 457, L57
 Kauffmann G., Melott A. L., 1992, *ApJ*, 393, 415
 Kim T. ., Bolton J. S., Viel M., Haehnelt M. G., Carswell

- R. F., 2007, ArXiv e-prints 0711.1862, 711
- Kim T., Hu E. M., Cowie L. L., Songaila A., 1997, *AJ*, 114, 1
- Kim T.-S., Cristiani S., D’Odorico S., 2001, *A&A*, 373, 757
- Kim T.-S., Viel M., Haehnelt M. G., Carswell B., Cristiani S., 2004a, *MNRAS*, 351, 1471
- Kim T.-S., Viel M., Haehnelt M. G., Carswell R. F., Cristiani S., 2004b, *MNRAS*, 347, 355
- Kirkman D., Tytler D., 1997, *ApJ*, 484, 672
- Kirkman D., Tytler D., Lubin D., Charlton J., 2007, *MNRAS*, 376, 1227
- Kirkman D., Tytler D., Suzuki N., Melis C., Hollywood S., James K., So G., Lubin D., Jena T., Norman M. L., Paschos P., 2005, *MNRAS*, 360, 1373
- Kohler K., Gnedin N. Y., 2007, *ApJ*, 655, 685
- Kritsuk A. G., Padoan P., Wagner R., Norman M. L., 2007, ArXiv e-prints, 706
- Lacey C., Cole S., 1994, *MNRAS*, 271, 676
- Lanzetta K. M., 1991, *ApJ*, 375, 1
- Lukic Z., Heitmann K., Habib S., Bashinsky S., Ricker P. M., 2007, ArXiv Astrophysics e-prints
- Mandelbaum R., McDonald P., Seljak U., Cen R., 2003, *MNRAS*, 344, 776
- McDonald P., 2003, *ApJ*, 585, 34
- McDonald P., Miralda-Escudé J., 2001, *ApJ*, 549, L11
- McDonald P., Miralda-Escudé J., Cen R., 2002, *ApJ*, 580, 42
- McDonald P., Miralda-Escudé J., Rauch M., Sargent W. L. W., Barlow T. A., Cen R., Ostriker J. P., 2000, *ApJ*, 543, 1
- McDonald P., Seljak U., Burles S., et al., 2006, *ApJS*, 163, 80
- Meiksin A., White M., 2004, *MNRAS*, 350, 1107
- Miralda-Escudé J., Rees M., 1994, *MNRAS*, 266, 343
- Misawa T., Tytler D., Iye M. Paschos P., Norman M., Kirkman D., O’Meara J., Suzuki N., Kashikawa N., 2004, *AJ*, *astroph/0303476*, 128, 2954
- Neto A. F., Gao L., Bett P., Cole S., Navarro J. F., Frenk C. S., White S. D. M., Springel V., Jenkins A., 2007, ArXiv e-prints, 706
- Norman M. L., Bryan G. L., 1999, in *ASSL Vol. 240: Numerical Astrophysics Cosmological Adaptive Mesh Refinement*. p. 19
- Norman M. L., Bryan G. L., Harkness R., Bordner J., Reynolds D., O’Shea B., Wagner R., 2007, ArXiv e-prints 0705.1556, 705
- O’Meara J. M., Prochaska J. X., Burles S., Prochter G., Bernstein R. A., Burgess K. M., 2007, *ApJ*, 656, 666
- O’Shea B. W., Bryan G., Bordner J., Norman M. L., Abel T., Harkness R., Kritsuk A., 2004, in *Adaptive Mesh Refinement – Theory and Applications*. Eds. T. Plewa, T. Linde & V.G. Weirs, Springer Lecture Notes in Computational Science and Engineering. Introducing ENZO, an AMR cosmology application
- O’Shea B. W., Nagamine K., Springel V., Hernquist L., Norman M. L., 2005, *ApJS*, 160, 1
- Paschos P., Norman M. L., Bordner J. O., Harkness R., 2007, ArXiv e-prints 0711.1904
- Pen U.-L., 1997, *ApJ*, 490, L127
- Petitjean P., Webb J. K., Rauch M., Carswell R. F., Lanzetta K., 1993, *MNRAS*, 262, 499
- Regan J. A., Haehnelt M. G., Viel M., 2007, *MNRAS*, 374, 196
- Sargent W., Young P., Boksenberg A., Tytler D., 1980, *ApJS*, 42, 41
- Sargent W. L. W., Steidel C. C., Boksenberg A., 1989, *ApJS*, 69, 703
- Schaye J., 2001, *ApJ*, 559, 507
- Schaye J., Aguirre A., Kim T.-S., Theuns T., Rauch M., Sargent W. L. W., 2003, *ApJ*, 596, 768
- Seljak U., Makarov A., McDonald P., and others 2005, *PhysRevD*, 71, 3515
- Sirko E., 2007, PhD thesis, Princeton University
- Slosar A., McDonald P., Seljak U., 2007, *New Astronomy Review*, 51, 327
- Stengler-Larrea E. A., Boksenberg A., Steidel C. C., Sargent W. L. W., Bahcall J. N., Bergeron J., Hartig G. F., Jannuzi B. T., Kirhakos S., Savage B. D., Schneider D. P., Turnshek D. A., Weymann R. J., 1995, *ApJ*, 444, 64
- Theuns T., Leonard A., Schaye J., Efstathiou G., 1999, *MNRAS*, 303, L58
- Tytler D., 1981, *Nature*, 291, 289
- Tytler D., 1982, *Nature*, 298, 427
- Tytler D., Kirkman D., O’Meara J., Suzuki N., Orin A., Lubin D., Paschos P., Jena T., Lin W.-C., Norman M., 2004, *ApJ*, 617, 1
- Tytler D., Kirkman D., O’Meara J. M., Suzuki N., Orin A., Lubin D., Paschos P., Jena T., Lin W., Norman M. L., Meiksin A., 2004, *ApJ*, 617, 1
- Viel M., Becker G. D., Bolton J. S., Haehnelt M. G., Rauch M., Sargent W. L. W., 2007, ArXiv e-prints 0709.0131
- Viel M., Haehnelt M., Carswell R., Kim T., 2003, *astro-ph/0308078* (relevant Fig missing from published version)
- Viel M., Haehnelt M. G., Lewis A., 2006, *MNRAS*, 370, L51
- Weymann R. J., Jannuzi B. T., Lu L., Bahcall J. N., Bergeron J., Boksenberg A., Hartig G. F., Kirhakos S., Sargent W. L. W., Savage B. D., Schneider D. P., Turnshek D. A., Wolfe A. M., 1998, *ApJ*, 506, 1
- Zhang Y., Anninos P., Norman M. L., Meiksin A., 1997, *ApJ*, 485, 496

APPENDIX A: HOW WE MAKE FLUX SPECTRA

We calculate the optical depth $\tau(v)$ using equations in §4 of J05, and the flux from $F = \exp(-\tau)$, where $F = 1.0$ in the absence of absorption. The spectra from all simulations are smooth functions of v , with no discreteness from the cell size, because to determine τ at each position we integrate over at least ± 600 cells to the left and right of the absorbing cell. At ≈ 5 km/s velocity resolution at $z=2$ this corresponds to an integration range of at least 6000 km/s. The number of cells involved in the integration can be larger if the absorption is to be computed on a high density location which can be a source of broad line wings.

The bulk of the spectra that we present here, unlike those in J05, were made at a fixed redshift. These spectra are frozen in time, as if made by light travelling infinitely fast at the chosen z . We convert from the Mpc per grid cell into velocity v in km s^{-1} of a spectrum using the $H(z)$ for the chosen z , but we do not increment the z as we move down a sight line, and we do not change the $H(z)$. These frozen

spectra are pixel to pixel identical if we pass through the box from the top to the bottom or in the reverse direction.

Each spectrum starts at a location of a face of the box and spans the length of the simulation to the opposite face along the z-direction. We made N^2 spectra that filled one side of the box, and as for the CDM, have explored the other two orthogonal directions and find it made very little difference to our output.

We encountered two problems with the spectrum generator. We initially truncated the integrations of the H I number density to obtain the opacity at $\pm 500 \text{ km s}^{-1}$ which lead to sharp cutoffs in the edges of the lines when high density cells first enter or leave an integration. In J05 we truncated at ± 200 cells, which was approximately 250 km s^{-1} in the highest resolution simulation (B2) and 2000 km s^{-1} for the A series. The second problem was an error in the spectrum generator which made it fail when the optical depth exceeded 10^7 , giving a near vertical spike in the spectrum. The first problem made the power spectra in all simulations turn up to higher than correct power on scales near the Nyquist frequency. The second problem effected 15 spectra from the A simulations alone, since the others did not have such high optical depths. We do not expect the last problem to have affected the results in J05 because we most likely did not sample high density regions with our random lines of sight. However, we believe that the limited integration range could have contaminated the spectra we reported in J05 and may explain some of the odd behaviour of the flux power.

APPENDIX B: EVOLVING SPECTRA

In addition to the spectra that we have discussed so far, all frozen in time, we also made spectra that include an approximation to the evolution expected in the IGM as light travels to us. The matter power in the IGM increases with decreasing z while the flux power decreases because the mean amount of absorption drops rapidly (Weymann et al. 1998; Janknecht et al. 2006; Kirkman et al. 2007). These changes will produce some power on their own, since they make the signals (matter density, flux, flux power) non-stationary, because they change systematically with z .

The evolving spectra are intended to mimic the cosmological evolution of the IGM as seen in QSO spectra. The parameters of the simulation are read out and stored for some z , and we then make the evolutions using scaling laws applied as the rays propagate through the data dump. We leave the radiation intensity constant, we scale the matter density as $(1+z)^3$ and the velocities as $(1+z)$. The ionization then increases with z . Since the redshift increments as we move along a sight line, we obtain different spectra if we reverse our direction of passage through the box.

Over the length of a single box, the evolution is unlikely to be significant. For example, crossing the A box, the redshift change is 0.05 and the mean flux changes by 0.004, with is about half of the measurement errors with current spectra. Moreover, we see ten times smaller change in the mean flux when we average over a range of redshifts that are symmetric about the central redshift: the evolution of the mean flux with z is nearly linear over small intervals. However, evolution is useful if we intend to traverse many

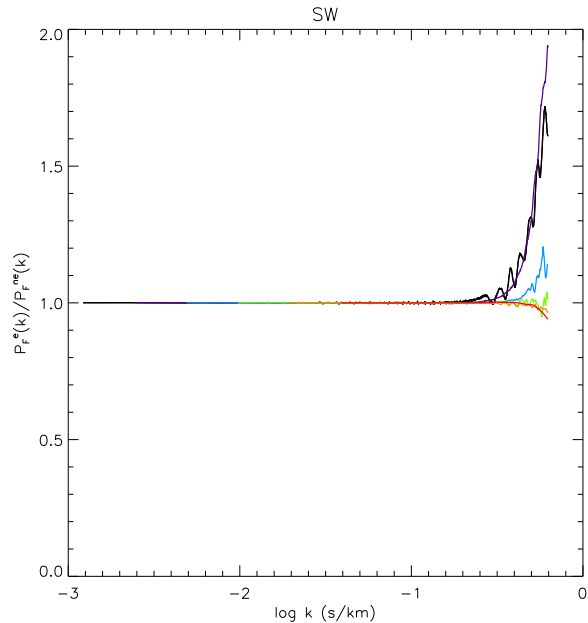


Figure B1. The effect of cosmological evolution along the sight lines on the power of the flux. We plot the ratio of the power of the spectra with evolution to the same without evolution.

data dumps at different redshifts, since with evolution we can more readily make smoothly evolving spectra.

In Fig. B1 we show the power of the flux from evolving spectra divided by the same for the stationary spectra that we have used up to now. The values for both the evolving and non-evolving power spectra were given in Table 9, Evolution has a dramatic effect on power spectra at high frequencies obtained using the FFT algorithm. The mean flux is different at either end of an evolving spectrum, and hence the spectrum itself will not join, but instead has a flux jump. When the box edge is in the wings of a line, this jump can be 5% in flux. These jumps can increase the power in a single spectrum at frequencies within a factor of a few of the Nyquist frequency by orders of magnitude, and increase the mean power from all sight lines by ten times.

One way to recover the expected power from spectra with evolution is to use a non-FFT algorithm. The evolution has an extremely mild effect on the flux and the conversion from Mpc into velocity. Both change slowly with velocity, in ways that have almost no effect on the small scale power. The effects that we show in Fig. B1 are artifacts of the use of the FFT on data with a discontinuity. To avoid the artifact, we could fit and remove the long term trends in the spectra before using the FFT, we can use a non-FFT algorithm, or we can window the data reducing the signal to zero at either end of each spectrum. In Fig. B2 we see that applying a Welch type window before using the FFT removes nearly all the artifacts.

APPENDIX C: EXTENDED SIGHT LINES IN RANDOM DIRECTIONS

We made all the spectra that we discussed so far parallel to the edges of a box, with the length of the box edge.

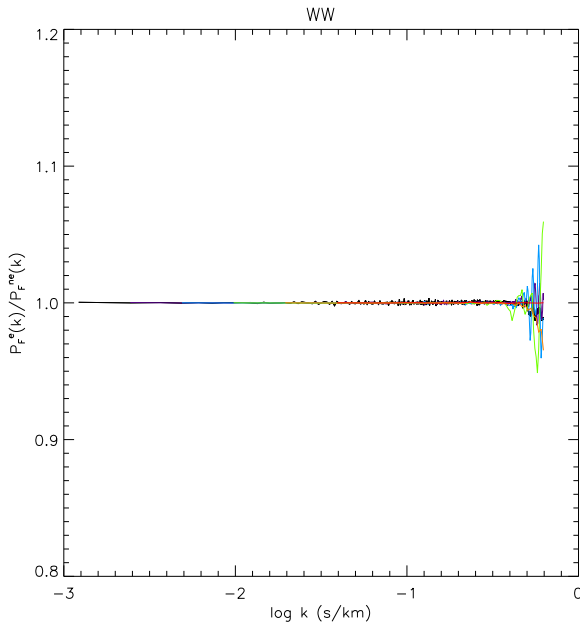


Figure B2. As Fig. B1 but after applying a Welch type window to both the evolving and non-evolving flux spectra.

We now discuss spectra that we made that can be of arbitrary length, by passing through the box multiple times in random directions. We can begin these spectra at random places in the simulation box, and send them in random directions. They loop through the simulation cube following the periodic boundary conditions, so that all the fields that specify the simulation vary smoothly and continuously along the sight line. A sight line that exits a face at 30 degrees to the normal will enter the opposite face travelling in the original direction, and in general the spectra do not duplicate. Since the direction is random, we interpolate the pixel values using a spline fit.

We have two methods of simulations evolution along these sight lines. For short sight lines, say $\delta z = 0.1$ we use the passive cosmological evolution that we described in §B. For longer sight lines we can patch together the data dumps from the simulation for different redshifts. When combined with the passive evolution, this allows us to make spectra that are as long as the forest of a single QSO. These spectra do not capture the full variation expected of the QSO sight line, because we have only a single volume evolving in time. However they are helpful, for example because they can contain the entire line from the DLA with a high N_{HI} , a line that can make the flux zero across entire sight line from a small box.

APPENDIX D: LACK OF REALISTIC VARIATION IN THE SIMULATIONS

When we compare to data, we are conscious that the simulation boxes have less variation for many connected reasons. We can see this difference by eye since the simulated spectra are more uniform and lack the large variations and strong clumping that we see in real spectra with the same total absorption from the low density Ly α forest alone. This com-

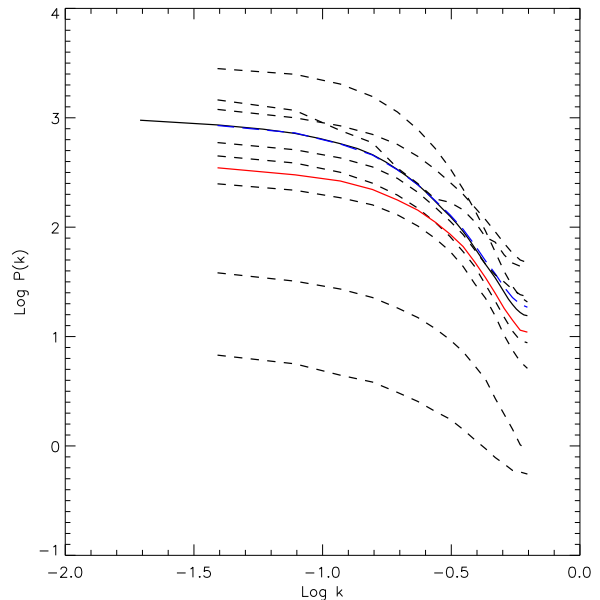


Figure D1. The 1D power spectra of δ_{CDM-1} for sight lines that fill each of the eight sub-cubes that exactly fill the A6 simulation. Each sub-cube has the same volume of A7, but unlike A7, the sub-cubes are not periodic, and they do not have the mean power or the mean density of the universe. The solid (blue) line extending farthest to the left is the power for A6. The eight dashed lines show the power for the sub-cubes. The short solid (red) line is the power for the A7 box.

parison is difficult because the real spectra include strong Ly α lines and metals that we need to mask and ignore.

At the physical level, our simulations all have identical ionizing radiation, both within the volume of each box and from box to box. They have exactly the mean density of the universe, and they begin with the mean power of the universe. Because of the periodic boundary conditions, they contain only modes that fit inside the box. All the simulations shown here have the same random number seed for the initial phases of their power.

In Figure D1 we see the power of δ_{CDM} for each of the eight sub-cubes that exactly fill simulation A6. Each sub-cube has the same volume as A7, and the same number and length of sight lines, but unlike A7, these sub-cubes are not periodic, they do not have the mean density of the universe, and they did not begin with the mean power in the universe. The amplitudes of the power spectra in the sub-cubes differ by many orders of magnitude. This is much more variation than seen in Figure 6 where we selected sight lines at random from all eight sub-cubes. The variation in density amongst the sub-cubes is large and it has a large effect on the power.

In Figure D2 we show the strong correlation between the mean density in a sub-cube and the variance of the δ_{CDM} . There is a very large variation in the mean density amongst the sub-cubes because they are only 2.4 Mpc on a side.

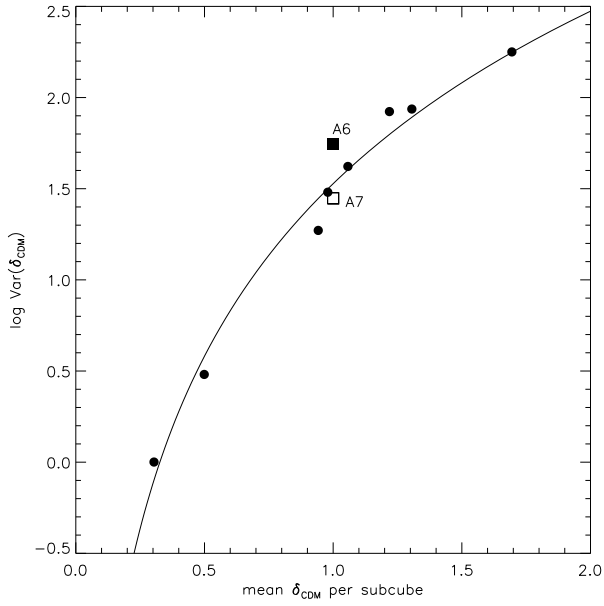


Figure D2. The variance of δ_{CDM} in sub-cubes of A6 as a function of their mean δ_{CDM} . We show the log of the mean of the dark matter variance values vertically, and the mean δ_{CDM} horizontally. Each circle applies to one of the eight sub-cubes that together fill A6 exactly. Each sub-cube has the same volume of A7. A7 is shown by the open square symbol and A6 by the filled square symbol, both at $\delta_{CDM}=1.0$.